

1 **Towards a satellite formaldehyde – in situ hybrid estimate for**
2 **organic aerosol abundance**

3
4 Jin Liao^{1,2}, Thomas F. Hanisco¹, Glenn M. Wolfe^{1,3}, Jason St. Clair^{1,3}, Jose L. Jimenez^{4,5},
5 Pedro Campuzano-Jost^{4,5}, Benjamin A. Nault^{4,5}, Alan Fried⁶, Eloise A. Marais^{7,*},
6 Gonzalo Gonzalez Abad⁸, Kelly Chance⁸, Hiren T. Jethva^{1,2}, Thomas B. Ryerson⁹,
7 Carsten Warneke^{9,5}, Armin Wisthaler^{10,11}

8
9 ¹Atmospheric Chemistry and Dynamic Laboratory, NASA Goddard Space Flight Center,
10 Greenbelt, MD, USA

11 ²Universities Space Research Association, GESTAR, Columbia, MD, USA

12 ³University of Maryland Baltimore County, Joint Center for Earth Systems Technology,
13 Baltimore, MD, USA

14 ⁴Department of Chemistry, University of Colorado, Boulder, Colorado, USA

15 ⁵Cooperative Institute for Research in the Environmental Sciences, University of
16 Colorado, Boulder, Colorado, USA

17 ⁶Department of Atmospheric and Oceanic Sciences, University of Colorado Boulder,
18 Boulder, Colorado, USA

19 ⁷School of Geography, Earth and Environmental Sciences, University of Birmingham,
20 UK

⁸Harvard-Smithsonian Center for Astrophysics, Cambridge, Massachusetts, USA

21 ⁹NOAA Earth System Research Laboratory (ESRL), Chemical Sciences Division,
22 Boulder, CO, USA

23 ¹⁰Department of Chemistry, University of Oslo, Oslo, Norway

24 ¹¹Institute for Ion Physics and Applied Physics, University of Innsbruck, Innsbruck,
25 Austria

26 *now at Department of Physics and Astronomy, University of Leicester, Leicester, UK

27
28
29
30 Correspondence email: jin.liao@nasa.gov

31 **Abstract**

32 Organic aerosol (OA) is one of the main components of the global particulate burden and
33 intimately links natural and anthropogenic emissions with air quality and climate. It is
34 challenging to accurately represent OA in global models. Direct quantification of global
35 OA abundance is not possible with current remote sensing technology; however, it may
36 be possible to exploit correlations of OA with remotely observable quantities to infer OA
37 spatiotemporal distributions. In particular, formaldehyde (HCHO) and OA share common
38 sources via both primary emissions and secondary production from oxidation of volatile
39 organic compounds (VOCs). Here, we examine OA-HCHO correlations using data from
40 summer time airborne campaigns investigating biogenic (NASA SEAC⁴RS and DC3),
41 biomass burning (NASA SEAC⁴RS) and anthropogenic conditions (NOAA CalNex and
42 NASA KORUS-AQ). In situ OA correlates well with HCHO ($r = 0.59 - 0.97$), and the
43 slope and intercept of this relationship depend on the chemical regime. For biogenic and
44 anthropogenic regions, the OA-HCHO slopes are higher in low NO_x conditions, because
45 HCHO yields are lower and aerosol yields are likely higher. The OA-HCHO slope of
46 wild fires is over 9 times higher than that for biogenic and anthropogenic sources. The
47 OA-HCHO slope is higher for highly polluted anthropogenic sources (e.g., KORUS-AQ)
48 than less polluted (e.g., CalNex) anthropogenic sources. Near-surface OA over the
49 continental US are estimated by combining the observed in situ relationships with HCHO
50 column retrievals from NASA's Ozone Monitoring Instrument (OMI). HCHO vertical
51 profiles used in OA estimates are from climatology a-priori profiles in the OMI HCHO
52 retrieval or output of specific period from a newer version of GEOS-Chem. Our OA
53 estimates compare well with US EPA IMPROVE data obtained over summer months

54 (e.g., slope = 0.60-0.62, $r = 0.56$ for August 2013), with correlation performance
55 comparable to intensively validated GEOS-Chem (e.g., slope = 0.57, $r = 0.56$) with
56 IMPROVE OA and superior to the satellite-derived total aerosol extinction ($r = 0.41$)
57 with IMPROVE OA. This indicates that OA estimates are not very sensitive to these
58 HCHO vertical profiles and that a priori profiles from OMI HCHO retrieval have a
59 similar performance to that from the newer model version in estimating OA. Improving
60 the detection limit of satellite HCHO and expanding in situ airborne HCHO and OA
61 coverage in future missions will improve the quality and spatiotemporal coverage of our
62 OA estimates, potentially enabling constraints on global OA distribution.

63 **1. Introduction**

64

65 Aerosols are the largest source of uncertainty in climate radiative forcing (IPCC 2013;
66 Carslaw et al., 2013) and decrease atmospheric visibility and impact human health (Pope
67 2002). Organic aerosols (OA) comprise a large portion (~50%) of submicron aerosols
68 (Jimenez et al., 2009; Murphy et al., 2006; Shrivastava et al., 2017), and this fraction will
69 grow with continued decline in SO₂ emissions (Attwood et al., 2014; Marais et al., 2017;
70 Ridley et al., 2018). In addition, OA serve as cloud condensation nuclei (CCN) and affect
71 cloud formation and climate radiative forcing. OA components also have adverse health
72 effects (e.g., Walgraeve et al., 2010) and contribute significantly to regional severe haze
73 events (e.g., Hayes et al., 2013). Finally, because the response of temperature to changes
74 in climate forcing is non-linear (Taylor and Penner, 1994) and the forcing by aerosols has
75 strong regional character (Kiehl and Briegleb, 1993), it is necessary to separate out
76 different climate forcing components to accurately forecast the climate response to
77 changes in forcing.

78

79 Despite their importance, it has been challenging to accurately represent OA in global
80 models. Chemical transport models (CTMs) often under-predict OA (e.g., more than a
81 factor of 2 lower OA near the ground) compared to observations, and model-to-model
82 variability can exceed a factor of 100 in the free troposphere (Tsigaridis et al., 2014;
83 Heald et al., 2008; Heald et al., 2011). Fully explicit mechanisms have attempted to
84 capture the full OA chemical formation mechanisms (e.g., Lee-Taylor et al., 2015), but it
85 is too computationally expensive to apply these mechanisms to OA formation in global
86 CTMs at a useful resolution. For computational efficiency, 3-D models such as GEOS-

87 Chem include direct emissions of primary OA (POA) and represent secondary OA (SOA)
88 formation either by lumping SOA products according to similar hydrocarbon classes
89 (Kim et al., 2015) or based on the volatility of the oxidation products (Pye et al., 2010).
90 Marais et al. (2016) applied an aqueous phase mechanism for SOA formation from
91 isoprene in GEOS-Chem to reasonably simulate isoprene SOA in the southeastern (SE)
92 US. Schroder et al. (2018) showed GEOS-Chem has a very large under prediction of
93 SOA in the Northeastern US dominated by anthropogenic emissions. Accurate emission
94 inventories are also needed to correctly represent volatile organic compounds (VOCs)
95 and NO_x (NO_x = NO + NO₂) inputs, and these often have biases compared to
96 observational constraints (Kaiser et al., 2018, Travis et al., 2016, Anderson et al., 2014;
97 McDonald et al., 2018).

98

99 A quantitative measure of OA from space would be helpful for verifying emissions and
100 aerosol processes in models. However, direct measurements of OA from space are
101 currently unavailable. Aerosol optical depth (AOD) measured by satellite sensors
102 provides a coarse but global picture of total aerosol distributions. Multi-angle Imaging
103 SpectroRadiometer (MISR) provides aerosol property information such as size, shape and
104 absorbing properties, which allows retrieving the AOD of a subset of aerosols (Kahn and
105 Gaitley, 2015). Classification algorithms have been developed to speciate different
106 aerosol types (e.g., OA) based on AOD, extinction Angstrom exponent, UV Aerosol
107 Index, and trace gas columns from satellite instruments (de Vries et al., 2015). Here we
108 aim to provide a quantitative estimation of OA mass concentrations from satellite
109 measurements.

110

111 Formaldehyde (HCHO) is one of the few VOCs that can be directly observed from space.
112 Sources emitting POA (e.g., biomass burning (BB)) often simultaneously release VOCs.
113 HCHO and SOA are also both produced from emitted VOCs. VOCs, as well as
114 intermediate- and semi- volatile organic compounds (I/SVOCs), are oxidized by hydroxyl
115 radicals (OH) to form peroxy radicals (RO₂), which then react with NO, RO₂, or
116 hydroperoxy radicals (HO₂) or isomerize. These oxidation processes produce HCHO and
117 oxidized organic compounds with low volatility that condense to form SOA (Robinson et
118 al., 2013; Ziemann and Atkinson, 2012). The yield of HCHO and SOA from hydrocarbon
119 oxidation thus depends on the VOC precursors, oxidants (OH, O₃ and NO₃), RO₂ reaction
120 pathway (e.g., NO levels), and pre-existing aerosol abundance and properties (Wolfe et
121 al., 2016; Pye et al., 2010; Marais et al., 2016 and 2017; Xu et al., 2016). Moreover,
122 although the lifetime of HCHO (1-3 hrs) is shorter than OA (1 week), HCHO continues
123 to form from slower reacting VOCs, as well as from the oxidation of later generation
124 products. Observations across megacities around the world show that OA formation in
125 polluted/urban area happens over about 1 day (e.g., DeCarlo et al., 2010; Hodzic and
126 Jimenez, 2011; Hayes et al., 2013; 2015), and HCHO is also significantly formed over
127 this timescale (Nault et al., 2018). In addition, Veeffkind et al. (2011) found that satellite
128 AOD correlated with HCHO over the summer time SE US, BB regions, and Southeast
129 Asian industrialized regions. This also suggests that OA share common emission sources
130 and photochemical processes with HCHO and are a major contributor to AOD in the
131 regions above. Marais et al. (2016) further used the relationship between aircraft OA and

132 satellite HCHO to evaluate GEOS-Chem representation of SOA mass yields from
133 biogenic isoprene in the SE US.

134

135 We present an OA surface mass concentration estimate (OA estimate) derived from a
136 combination of satellite HCHO column observations and in situ OA-HCHO relationships.

137 Because the detection limit of satellite HCHO column observations limit the quality of
138 OA estimate, we focus our analyses on summer time when HCHO levels are high. The
139 OA estimate is evaluated against OA measurements at ground sites. A 3-D model GEOS-
140 Chem OA simulation is shown for comparison.

141

142 **2. Methods**

143 **2.1 In situ airborne observations**

144 Figure 1 shows flight tracks with altitudes < 1 km of the field campaigns used in the
145 current study. The Studies of Emissions, Atmospheric Composition, Clouds and Climate
146 Coupling by Regional Surveys (SEAC⁴RS) mission (Toon et al., 2016) covered the
147 continental US with a focus on the SE US in August-September 2013. The Deep
148 Convective Clouds & Chemistry Experiment (DC3) (Barth et al., 2015) surveyed the
149 central and SE US in May-June 2012, targeting isolated deep convective thunderstorms
150 and mesoscale convective systems. The California Research at the Nexus of Air Quality
151 and Climate Change (CalNex) (Ryerson et al., 2013) investigated the California region in
152 May-June 2010, targeting the Los Angeles (LA) Basin and Central Valley. The Korea-
153 United States Air Quality Study (KORUS-AQ) studied South Korean air quality,
154 sampling many large urban areas in South Korea and continental Asian outflow over the

155 West Sea, in May-June 2016 (Aknan and Chen, 2017). KORUS-AQ only includes data
156 with longitude $< 133^{\circ}$ E to exclude the transit from US because it targeted South Korea
157 and the nearby region. These field campaigns were selected as they had recent high-
158 quality in situ HCHO and OA data measured with state-of-the-art instruments and studied
159 summer time regional tropospheric chemical composition.

160

161 In situ airborne HCHO observations were acquired by multiple instruments. The DC3
162 NASA DC-8 payloads featured two HCHO measurements: the NASA In Situ Airborne
163 Formaldehyde (ISAF) (Cazorla et al., 2015) and the Difference Frequency Generation
164 Absorption Spectrometer (DFGAS) (Weibring et al., 2006). The SEAC⁴RS NASA DC-8
165 payloads also featured two HCHO measurements: the NASA ISAF and the Compact
166 Atmospheric Multispecies Spectrometer (CAMS) (Richter et al., 2015). HCHO
167 measurements from ISAF were found to be in good agreement with CAMS, with a
168 correlation coefficient of 0.99 and a slope of 1.10 (Zhu et al., 2016). HCHO
169 measurements from ISAF also had a good agreement with DFGAS, with a correlation
170 coefficient of 0.98 and a slope of 1.07. Because ISAF has higher data density, we used
171 ISAF HCHO data for DC3 and SEAC⁴RS. During KORUS-AQ, CAMS was the only
172 HCHO instrument onboard the DC-8. In CalNex a proton transfer reaction mass
173 spectrometer (PTR-MS) (Warneke et al., 2011) was used to measure HCHO on board the
174 NOAA P3 aircraft.

175

176 In situ airborne OA from SEAC⁴RS, DC3, and KORUS-AQ was measured by the
177 University of Colorado High-Resolution Time-of-Flight Aerosol Mass Spectrometer

178 (AMS, DeCarlo et al., 2006; Dunlea et al., 2009; Canagaratna et al., 2007; Jimenez et al.,
179 2016) and in situ airborne OA from CalNex was measured by the NOAA Compact Time-
180 of-Flight Aerosol Mass Spectrometer (Drewnick et al., 2005; Canagaratna et al., 2007;
181 Bahreini et al., 2012). The OA measurements are from 1 min merge data and converted
182 from $\mu\text{g sm}^{-3}$ (at 273 K and 1013 mbar) to $\mu\text{g m}^{-3}$ under local T & P for each data point,
183 to be consistent with HCHO concentrations in $\mu\text{g m}^{-3}$ or molec cm^{-3} at local T & P.

184

185 Although NO modulates the RO_2 lifetime, and thus, the production of HCHO and SOA,
186 NO cannot be directly observed via remote sensing. Instead, NO_2 can be directly
187 observed in space by satellites, and because NO_2 represents typically ~80% (e.g.,
188 SEAC⁴RS and KORUS-AQ) of the boundary layer NO_x concentrations during the
189 daytime, NO_2 can be used as a surrogate for daytime NO concentrations and oxidative
190 conditions around the globe. In situ airborne NO_2 was measured by the NOAA
191 Chemiluminescence NO_yO_3 instrument (Ryerson et al., 2001) during SEAC⁴RS, DC3,
192 and CalNex and by University of Berkeley laser induced fluorescence NO_2 instrument
193 (Day et al., 2002) during KORUS-AQ. SEAC⁴RS isoprene measurements were from
194 proton-transfer-reaction mass spectrometer (PTR-MS) (Wisthaler et al., 2002).

195

196 **2.2 Ground-based OA measurements**

197 Ground-based OA measurements over the US were from the EPA Interagency
198 Monitoring of Protected Visual Environments (IMPROVE) (Malm et al., 1994; Solomon
199 et al., 2014; Hand et al., 2014; Hand et al., 2013; Malm et al., 2017) and Southeastern
200 Aerosol Research and Characterization (SEARCH) (Edgerton et al., 2006) networks. In

201 the IMPROVE network, aerosols were collected on quartz fiber filters and analyzed in
202 the lab by thermal optical reflectance for organic and elemental carbon. The data were
203 reported every three days from 1988 to 2014. Monthly averages were used for
204 comparison in this study. IMPROVE OA data over the SE US (east of 70°W) in summer
205 time were multiplied by a factor of 1.37 to correct for partial evaporation during filter
206 transport, following the recommendation of a comparison study with SEARCH organic
207 carbon (OC) measurements (Kim et al., 2015; Hand et al., 2013). Although IMPROVE
208 OA corrected for evaporation has potential uncertainties with the constant scaling factor,
209 the IMPROVE measurements have high spatial coverage. SEARCH network (Edgerton
210 et al., 2006; Hidy et al., 2014) OC was determined by the difference between total carbon
211 (TC) detected by a tapered element oscillating microbalance (TEOM) and black carbon
212 (BC) measured by an in situ Thermal Optical instrument. This allowed real-time
213 measurement of OC and prevented evaporation during filter transport. Although the
214 SEARCH network only has 5 sites available, we used observations from this network due
215 to their high accuracy. The IMPROVE and SEARCH network OC measurements were
216 converted to OA by multiplying by a factor of 2.1 based on ground and aircraft
217 observations (Pye et al., 2017; Schroder et al., 2018).

218

219 **2.3 Satellite measurements**

220 Satellite HCHO column observations were derived from the NASA's Ozone Monitoring
221 Instrument (OMI), a UV/Vis nadir solar backscatter spectrometer on the Aura satellite
222 (Levelt et al., 2006). Aura overpasses the equator at 1:30 pm local time, daily. Here we
223 used the OMI HCHO version 2.0 (collection 3) gridded ($0.25^\circ \times 0.25^\circ$) retrieval data

224 (Gonzalez Abad et al., 2015) from the Smithsonian Astrophysical Observatory (SAO).
225 Satellite data for HCHO columns were subjected to data quality filters: 1) solar zenith
226 angle lower than 70° , 2) cloud fraction less than 40%, and 3) main quality flag and the
227 xtrackquality flag both equal to zero (Harvard-Smithsonia Center for Astrophysics OMI
228 HCHO data product description). The monthly average HCHO columns were also
229 weighted by the column uncertainties of the pixels. The HCHO retrieval used a priori
230 profiles without aerosol information from the GEOS-Chem model (Gonzalez Abad et al.,
231 2015). Satellite NO_2 column observations were also derived from NASA's OMI level 3
232 data (Lamsal et al., 2014; NASA OMI NO_2 data archive). Satellite NO_2 observations
233 were used to calculate NO_x related chemical factor dependent OA estimate (see Table 2).
234 Satellite AOD observations were acquired from the Moderate Resolution Imaging
235 Spectroradiometer (MODIS) onboard the Aqua satellite, using overpasses at about 1:30
236 pm local time. Here, we used collection 06 (NASA MODIS AOD data archive), retrieved
237 using the Dark Target (DT) and Deep Blue (DB) algorithms (Levy et al., 2015), monthly
238 average data.

239

240 **2.4 GEOS-Chem**

241 We used GEOS-Chem (v9-02) at $2^\circ \times 2.5^\circ$ with 47 vertical layers to simulate HCHO and
242 OA globally, the same as that in Marais et al. (2016). GEOS-Chem was driven with
243 meteorological fields from the NASA Global Modeling and Assimilation Office
244 (GMAO). The OA simulation included POA from fires and anthropogenic activity and
245 SOA from the volatility-based reversible partitioning scheme (VBS) of Pye et al. (2010)
246 for anthropogenic, fire, and monoterpene sources, and an irreversible aqueous-phase

247 reactive uptake mechanism for isoprene. The aqueous-phase mechanism was coupled to
248 gas-phase isoprene chemistry and has been extensively validated using surface and
249 aircraft observations of isoprene SOA components in the SE US (Marais et al., 2016).
250 This model version used the fourth-generation global fire emissions database (GFED4)
251 (Giglio et al., 2013) as BB emission inventory. The model was driven with Goddard
252 Earth Observing System – Forward Processing (GEOS-FP) meteorology for 2013 and
253 sampled along the SEAC⁴RS (2013) and KORUS-AQ (2016) flight tracks. The model
254 was also run with 10% decrease in biomass burning, biogenic, or anthropogenic
255 emissions as a sensitivity test to evaluate the contributions of different sources to OA and
256 HCHO budget. Model monthly mean surface layer OA and total column formaldehyde
257 were obtained around the OMI overpass time (12:00-15:00 local time) for 2008-2013
258 using Modern-Era Retrospective analysis for Research and Applications (MERRA)
259 (Gelaro et al., 2017) meteorology, as GEOS-FP was only available from 2012. This was
260 compared to the OA estimate derived from satellite HCHO.

261

262 Global isoprene emissions from the Model of Emissions of Gases and Aerosols from
263 Nature version 2.1 (MEGAN) (Guenther et al., 2006) and satellite NO₂ column data were
264 used to calculate an isoprene and NO₂ dependent OA estimate (see Table 2). Global
265 isoprene emissions from MEGAN were implemented in GEOS-Chem and driven with
266 MERRA (MEGAN-MERRA).

267

268 **2.5 Estimation of surface organic aerosol mass concentrations**

269 An estimate for surface OA mass concentration was calculated based on a simple linear
270 transformation.

$$271 \quad \varepsilon(i) = \Omega_{HCHO}(i)\eta(i)\alpha(i) + \beta(i) \quad \text{Eq. (1)}$$

272 Here, $\varepsilon(i)$ is the OA estimate for grid cell i ($\mu\text{g m}^{-3}$), $\Omega_{HCHO}(i)$ is the OMI HCHO column
273 density (molec cm^{-2}) in each $0.25^\circ \times 0.25^\circ$ grid cell (similar resolution to OMI HCHO
274 nadir pixel data), $\eta(i)$ is the ratio of midday surface layer (~ 60 m) HCHO concentrations
275 (molec cm^{-3}) to column concentrations (molec cm^{-2}) from GEOS-Chem, and $\alpha(i)$ and
276 $\beta(i)$ are the slope and intercept of a linear regression between OA and HCHO from low
277 altitude (< 1 km) airborne in situ measurements. The in situ to column conversion factor
278 $\eta(i)$ was similar to that used by Zhu et al. (2017) to convert HCHO columns into surface
279 concentrations. $\eta(i)$ was derived from the HCHO a priori profiles used in SAO OMI air
280 mass factor (AMF) calculations (GEOS-Chem v9-01-03 climatology) or from GEOS-
281 Chem v9-02, which included updated isoprene scheme for OA and is the next version of
282 the model (v9-01-03) for a priori profiles used in SAO satellite HCHO retrievals. HCHO
283 a priori profiles were used to be consistent with satellite HCHO retrievals and also to
284 show that OA estimate can be derived without running a global model separately. The
285 newer version of GEOS-Chem was used to test the sensitivity of OA estimates to updated
286 version of η . The newer version of GEOS-Chem also allows sampling through the flight
287 tracks of a recent field campaign (SEAC⁴RS) and examining the factors impacting η with
288 both modeled and measured HCHO profiles. The detailed information about the impact
289 of HCHO profiles on η is provided in Sect. 5.

290

291 **2.6 Aerosol extinction from satellite measurements**

292 Currently remote sensing techniques observe aerosols by quantifying AOD. The MISR
293 satellite instrument can estimate a subset of AOD, using constraints on size range, shape
294 and absorbing properties, but it cannot distinguish OA from other submicron aerosol
295 compounds such as sulfate and nitrate and also requires AOD to be above 0.1. Because
296 MISR estimates a subset of AOD, it is discussed above to verify that we are not
297 neglecting a satellite dataset that has already captured OA AOD. Moreover, OA account
298 for a large and relatively constant fraction of submicron aerosols in the SE US (Kim et
299 al., 2015; Wagner et al., 2015) and are one of the major submicron aerosol components
300 over the US (Jimenez et al., 2009). Therefore, AOD was converted to extinction to
301 represent OA for comparison.

$$302 \quad A_{ext} = AOD(i)\delta(i) \quad \text{Eq. (2)}$$

303 where A_{ext} is the calculated aerosol extinction (Mm^{-1}), $AOD(i)$ is aerosol optical depth
304 from MODIS (see Sect. 2.3) in each $0.25^\circ \times 0.25^\circ$ grid cell, and $\delta(i)$ (m^{-1}) is the ratio of
305 surface layer OA concentrations ($\mu g m^{-3}$, at ambient T & P) to column OA concentrations
306 ($\mu g m^{-2}$) from GEOS-Chem multiplied by $10^6 Mm^{-1}/m^{-1}$. The shape of the average
307 vertical profile of OA (OA fraction: 0.54-0.7) was close to that of total aerosol mass over
308 SE US (Wagner et al., 2015) where a large fraction of the enhanced non-BB aerosol
309 concentrations in summer time over the US are located. Data with BB plumes
310 interferences were excluded in the following analysis. The potential contribution of dust
311 and nitrate could alter the shape of the vertical profiles and introduce uncertainties when
312 using OA vertical profiles for other parts of the US. However, the outliers in the aerosol
313 extinction compared to ground OA measurements (see Sec. 6.3) were not located outside
314 of the SE US. Similar vertical profile shapes of OA and submicron particles were also

315 observed in a campaign outside the US over South Korea (Nault et al., 2018). Although
316 OA accounted for ~40% of the total submicron particles, the shape of OA and total
317 submicron particles vertical profiles were nearly identical.

318

319 **3. In situ OA-HCHO relationship**

320 Although OA and HCHO share common VOC emission sources and photochemical
321 processes, their production rates from different emission sources and photochemical
322 conditions vary, as do their loss rates. We found the main factors that modulate OA-
323 HCHO relationships from in situ measurements and discussed in the following section.

324

325 **3.1 Regional and Source-Driven Variability**

326 For all regions and/or sources investigated, near-surface in situ OA and HCHO are well
327 correlated. A scatter plot of in situ OA vs. HCHO at low altitudes (<1 km) from a number
328 of field campaigns (SEAC⁴RS, DC3, CalNex, and KORUS-AQ) is displayed in Fig. 2.
329 The slopes, intercepts, and correlation coefficients are summarized in Table 1. SEAC⁴RS,
330 DC3, and CalNex excluded BB data when acetonitrile > 200 pptv (Hudson et al., 2004).
331 KORUS-AQ used a BB filter with higher acetonitrile (>500 pptv) because the air masses
332 with moderate acetonitrile enhancement (200-500 pptv) were actually from
333 anthropogenic emissions. This attribution is based on high levels of acetonitrile detected
334 downwind of Seoul and west coastal petrochemical facilities, the slope between
335 acetonitrile and CO being to urban emissions (Warneke et al., 2006), and the
336 concentrations of anthropogenic tracer CHCl₃ being high (Warneke et al., 2006). Similar
337 to acetonitrile, another common BB tracer hydrogen cyanide (HCN) was also enhanced

338 in these air masses. BB data (acetonitrile > 200 pptv) for SEAC⁴RS were analyzed
339 separately and are inset in Fig. 2. Although all CalNex data had a tight correlation, we
340 only included the flight data near LA basin to target the area strongly influenced by
341 anthropogenic emissions. In general, the correlation coefficients between in situ OA and
342 HCHO were strong ($r = 0.59 - 0.97$) (Table 1).

343
344 The variety in OA-HCHO regression coefficients among different campaigns reflects the
345 regional and/or source-driven OA-HCHO variability. Considering only the non-biomass
346 burning (non-BB) air masses sampled, OA and HCHO had the tightest correlation for
347 CalNex, because CalNex focused on the LA area (shown in Fig. 2) and Central Valley
348 while SEAC⁴RS and DC3 covered a larger area with a potentially larger variety of
349 sources and chemical conditions. Although SEAC⁴RS and DC3 both sampled the
350 continental US, SEAC⁴RS had more spatial coverage and sampled more air masses at low
351 altitudes, while DC3 was designed to sample convective outflow air masses and had more
352 data at high altitudes. Although KORUS-AQ covered a much smaller area compared to
353 SEAC⁴RS, KORUS-AQ data also had a large spread, which may be due to the
354 complicated South Korean anthropogenic sources mixed with transported air masses
355 (e.g., from China) and maybe biogenic sources. OA exhibits a tight correlation with
356 HCHO for both wildfires and agricultural fires during SEAC⁴RS. This is because the
357 production of HCHO and OA is much higher in BB air masses compared to background.
358 This may also suggest that the emissions of OA and HCHO in these air masses are
359 relatively constant. SEAC⁴RS data are chosen because it sampled fires and had state-of-
360 the-art, high quality measurements. More intensive fire sampling is needed to probe the
361 correlation between OA and HCHO across fuel types and environmental conditions.

362
363 The different slopes of OA-HCHO among different campaigns also reflect the regional or
364 source-driven OA-HCHO variability. Among the BB, anthropogenic and biogenic
365 sources, the slopes of OA vs. HCHO for BB air masses were the highest. This is
366 consistent with high POA emission in BB conditions (Heald et al., 2008; Lamarque et al.,
367 2010; Cubison et al., 2011), with low addition of mass due to SOA formation (Cubison et
368 al., 2011; Shrivastava et al., 2017). The slope of OA to HCHO was higher for wildfires
369 than agricultural fires during SEAC⁴RS though data were limited (see Table 1). This is
370 consistent with more OA emitted in wildfires than agricultural fires (Liu et al., 2017).
371 The factors driving higher OA to HCHO with wildfires are not clear and may be related
372 to burning conditions and fuels. For the non-BB sources, the slope of OA vs. HCHO was
373 highest for South Korea (KORUS-AQ), which is dominated by heavily polluted
374 anthropogenic sources. During KORUS-AQ, the high OA to HCHO air masses also had
375 high acetonitrile. By the time we sampled, most organic aerosols were secondary (Nault
376 et al., 2018). This indicates that the formation rates of OA and HCHO from different
377 emission sources contribute to the different slopes of OA-HCHO. This also indicates that
378 emission sources with enhanced acetonitrile tend to form more OA relative to HCHO
379 downwind. The slope of OA-HCHO for California LA basin, dominated by relatively
380 clean anthropogenic emissions, was much lower than South Korea. The potential
381 difference in the anthropogenic emissions mix could contribute to the different OA-
382 HCHO slopes from US LA region and South Korea anthropogenic sources (Baker et al.,
383 2008; Na et al., 2005; Na et al., 2002). The slopes of OA vs. HCHO of SEAC⁴RS and
384 DC3 dominated by biogenic emissions in the SE US were in-between heavily polluted

385 (KORUS-AQ) and clean anthropogenic sources (CalNex). As SEAC⁴RS had the largest
386 geographic coverage for low altitude data over US, the campaign average slope of OA vs.
387 HCHO was used to represent the US region in summer. CalNex LA Basin data were used
388 to represent large cities as case studies.

389

390 Overall, the source dependent OA-HCHO relationships (Fig. 2) showed higher OA-
391 HCHO slopes of BB and heavily polluted anthropogenic sources with inefficient
392 combustion (e.g., KORUS-AQ) compared to biogenic and relatively clean anthropogenic
393 sources. This indicated that inefficient combustions contribute to the high slopes of OA-
394 HCHO, probably due to both enhanced primary OA and increased formation of SOA.
395 Enhanced pre-existing aerosols such as primary aerosols can provide more surfaces to
396 increase VOCs condensation and SOA formation. VOCs co-emitted from heavily
397 polluted anthropogenic sources can also form more SOA. It is possible to extract the
398 factors that govern the different OA-HCHO relationships and potentially have a universal
399 application of the slopes as a function of the factors (e.g., sources and combustion
400 efficiencies).

401

402 **3.2 Dependence on NO_x and VOCs speciation**

403 Biogenic and anthropogenic VOCs are oxidized by atmospheric oxidants (e.g., OH as the
404 dominant oxidant) to form RO₂. HCHO is produced from the reactions of RO₂ with HO₂
405 or NO, with RO₂+NO typically producing more HCHO than RO₂ + HO₂ (e.g., Wolfe et
406 al., 2016). RO₂ can react with HO₂ or NO, or isomerize to form oxidized organic
407 compounds with high molecular weight and low volatility, which condense on existing

408 particles to form SOA. The products of $\text{RO}_2 + \text{NO}$ tend to fragment instead of
409 functionalize and often lead to higher volatility compounds (e.g., HCHO) and thus less
410 SOA formation compared to the products of $\text{RO}_2 + \text{HO}_2$ (Kroll et al., 2006; Worton et al.,
411 2013). Therefore, with the same VOC, we expect more HCHO and less OA formed at
412 high NO conditions and vice versa. As mentioned before, NO_2 instead of NO is easily
413 measured from space and NO_2 typically is $\sim 80\%$ of NO_x in the boundary layer during the
414 day. Therefore, NO_2 is used as a surrogate for the NO levels influencing OA and HCHO
415 production. The yields of HCHO and SOA also depend on VOC speciation (e.g., Lee et
416 al., 2006; Bianchi et al., 2016). Specifically, isoprene has a higher yield of HCHO than
417 most non-alkene VOCs (Dufour et al., 2009).

418

419 A scatter plot of OA vs. HCHO for SEAC⁴RS low altitude data is shown in Fig. 3(a). The
420 data are color-coded by the product of in-situ isoprene and NO_2 , attempting to capture
421 time periods strongly influenced by oxidation products of isoprene at high NO
422 conditions. No trends are evident when the data are instead color coded by NO_2 or
423 isoprene only. This may be because isoprene (biogenic source) and NO_2 (anthropogenic
424 sources) are generally not co-located in the US (Yu et al., 2016) and isoprene is the
425 dominant source of HCHO compared to anthropogenic VOCs in the US (e.g., Millet et
426 al., 2008). This plot shows that, at high NO_2 and high isoprene conditions, less OA was
427 formed for each HCHO produced generally. The correlation coefficient of 0.45 for high
428 NO_2 and isoprene conditions during SEAC⁴RS is not very high but still shows significant
429 dependence of the OA-HCHO relationship on the product of NO_2 and isoprene,
430 considering that these are ambient data and other factors (e.g., different specific sources)

431 also play a role in determining OA-HCHO relationships. This is consistent with high NO
432 and isoprene conditions promote HCHO formation over SOA formation. We also looked
433 at the dependence on peroxy acetyl nitrate (PAN), as PAN is a product of the photo
434 oxidation of VOCs, including isoprene, in the presence of NO₂. The dependence on PAN
435 was not as clear as on the product of NO₂ and isoprene.

436

437 KORUS-AQ OA vs. HCHO, color-coded with NO₂, is plotted in Fig. 3(b). The OA-
438 HCHO ratio clearly decreased as NO₂ levels increased during KORUS-AQ, suggesting
439 that high NO conditions accelerated HCHO formation more than they did SOA
440 production. OA-HCHO relationships do not have dependence on local time of the day
441 (not shown). This further confirms that NO_x is an important factor that affects the OA-
442 HCHO relationship. Compared to SEAC⁴RS, the KORUS-AQ OA-HCHO ratio does not
443 depend on VOCs. This may be consistent with the dominant VOCs being anthropogenic
444 VOCs that are co-located with NO sources. This may also suggest that the anthropogenic
445 VOCs generally have a lower HCHO yield than does isoprene. Because OA and HCHO
446 were tightly correlated during CalNex and DC3, we did not parse for NO_x. The NO_x
447 range during DC3 low altitude data was smaller than KORUS-AQ and SEAC⁴RS. DC3
448 OA-HCHO relationships only had a slight dependence on NO₂ (not shown here), largely
449 due to the limited dataset. The NO_x range during CalNex low altitude data was large. The
450 OA and HCHO correlation during CalNex was very tight and the slope of OA-HCHO did
451 not show clear dependence on NO_x, which could be due to the combination of different
452 VOCs sources and NO_x levels.

453

454 **4. Comparison of OA-HCHO relationships: in-situ vs. GEOS-Chem**

455 In situ OA-HCHO relationships from SEAC⁴RS low altitude non-BB (Fig. 4a), KORUS-
456 AQ low altitude (Fig. 4b), and SEAC⁴RS BB (Fig. 4c) air masses were compared to
457 GEOS-Chem model simulations (Fig. 4d-4f) sampling along the corresponding flight
458 tracks. Similar to the in situ data, GEOS-Chem model simulations also found correlations
459 between OA and HCHO for these three regions, especially for SEAC⁴RS non-BB.
460 GEOS-Chem was intensively validated with in situ measurements for SE US (e.g.,
461 Marais et al., 2016; Kim et al., 2015). The ratios of the slopes between OA and HCHO
462 for the US (SEAC⁴RS), South Korea (KORUS-AQ), and wildfire cases (SEAC⁴RS) from
463 GEOS-Chem were 1:1.1:0.4, which was different from the in situ measurements of
464 1:1.4:13 (Table 1). GEOS-Chem could not capture any wild fires in US during
465 SEAC⁴RS, which is probably due to poor representation of BB emission inventory for US
466 wildfire and also the coarse grid in GEOS-Chem. GEOS-Chem also significantly under
467 predicted the slope of OA to HCHO for South Korea. We attribute this to a likely
468 underprediction of anthropogenic SOA, which was dominant in South Korea, in GEOS-
469 Chem (Schroder et al., 2018), as well as a different mix of OA and HCHO sources in the
470 US compared to South Korea and representation of these in GEOS-Chem. Although
471 GEOS-Chem contains isoprene chemistry with a focus on the SE US (Marais et al. 2016),
472 there is still room to improve GEOS-Chem model especially for anthropogenic and BB
473 sources, as well as anthropogenic OA formation mechanisms. For example, in the model
474 biogenic sources are more important than anthropogenic sources for the OA and HCHO
475 budgets in South Korea, which is not the case from KORUS-AQ in situ measurements. In
476 the model, a 10% decrease of emissions from biogenic, anthropogenic and BB sources

477 results in a 6%, 3%, and 1% decrease in OA and 2%, 1%, and 0% decrease in HCHO
478 over South Korea in May 2016. However, the in situ airborne field campaign KORUS-
479 AQ found that OA and HCHO were higher near anthropogenic emission sources
480 compared to rural regions. The larger impact of biogenic sources compared to
481 anthropogenic sources on OA and HCHO in the model can be due to both low-biased
482 anthropogenic emission inventories and low-biased anthropogenic SOA. Improving
483 anthropogenic emissions inventories in the models can bring model results closer to
484 observations. Improving anthropogenic SOA, such as implementation of the SIMPLE
485 model, in GEOS-Chem (Hodzic and Jimenez, 2011) can also improve the model results
486 compared to observations. Measurements or measurement-constrained estimation with
487 sufficient spatial and temporal coverage can help to narrow down the key factors (e.g.,
488 emission inventories or chemical schemes) in GEOS-Chem to better represent VOCs and
489 OA globally. Furthermore, we did also find that GEOS-Chem could not capture the
490 observed higher slope of OA to HCHO at high altitudes (not shown), which could be due
491 to issues such as transport, OA lifetime, and OA production.

492

493 **5. Relating satellite HCHO column to surface HCHO concentrations**

494 To utilize the derived in-situ OA-HCHO relationship, the satellite HCHO columns need
495 to be converted to surface HCHO concentrations. We used a vertical distribution factor η
496 (cm^{-1}) (Sect. 2.5), which is defined as the ratio of surface HCHO concentrations (molec
497 cm^{-3}) to HCHO column (molec cm^{-2}), to estimate surface HCHO concentrations from
498 satellite column measurements. Zhu et al. (2017) used the same vertical distribution
499 factor for their study. The use of this factor is justified by the fact that the derived surface

500 HCHO retained the spatial pattern of the satellite HCHO column and agreed with local
501 surface measurements of HCHO for a multi-year average (Zhu et al., 2017).
502
503 We also investigated the main factors affecting the variation of the vertical distribution
504 factor η . Because the factor is determined by HCHO vertical distributions, we examined
505 three typical normalized HCHO vertical distribution profiles with the highest, median and
506 lowest η values for the SEAC⁴RS field campaign (Fig. 5). Because the sensitivity of OA
507 estimates to η was investigated with η from different GEOS-Chem versions (Sect. 6.2),
508 we did not compare HCHO vertical profiles from the model to the measurements from a
509 comprehensive set of field campaigns. We chose SEAC⁴RS to illustrate the main factors
510 impacting the η over US because SEAC⁴RS had a larger spatial coverage than DC3 and
511 CalNex. GEOS-Chem can generally capture the vertical profiles of measured HCHO.
512 Boundary layer mixing height and surface emission strength are the dominant factors in
513 determining the fraction of HCHO near the surface. Higher boundary layer mixing height
514 results in lower η for SE US profiles, where there are biogenic sources of HCHO from
515 the surface and HCHO has distinct concentration difference below and above the
516 boundary layer. However, there are exceptions, such as for the profiles over the ocean
517 and the coastal regions. Although the boundary layer is shallow in these regions, a large
518 portion of HCHO resides above the boundary layer, resulting in low η . In these cases,
519 surface emissions of HCHO or precursors are very small and therefore methane oxidation
520 makes a large contribution to the total HCHO column. High concentrations of HCHO
521 (e.g., in BB plumes) lofted by convection can also impact the vertical profile (Barth et al.,
522 2015), which is not further investigated because OA estimates with BB influences over

523 US are excluded in current study. Overall, the source intensities and boundary layer
524 mixing height mostly determined the HCHO vertical profiles.

525

526 **6. Construction of the OA estimate**

527 **6.1 Variables to construct OA estimate**

528 As mentioned in Sect. 2.5, the OA estimate value in each grid cell was estimated from
529 monthly average satellite HCHO column observation by the linear Eq. (1). Satellite
530 monthly average HCHO column data, Ω_{HCHO} , were converted to surface HCHO
531 concentrations by multiplying by the $\eta(i)$ factor either from climatology a priori profiles
532 or monthly average HCHO profiles. Surface OA was then estimated by multiplying the
533 derived surface HCHO concentrations with the slope $\alpha(i)$ and adding the intercept $\beta(i)$.
534 The slope $\alpha(i)$ and intercept $\beta(i)$ were determined from the linear regression of in situ
535 OA and HCHO from aircraft field campaign data. The relationship between OA and
536 HCHO varies but previous sections demonstrated that we can quantify the surface OA-
537 HCHO relationship by their regions, sources and chemical conditions (e.g., NO_x and
538 isoprene levels). To test the impact of the chosen OA-HCHO relationship on the
539 calculated OA estimate, the OA estimate in the US was calculated using four different
540 methods (see Table 2). The OA estimate was calculated on the monthly time scale,
541 largely because OA estimate is based on OMI HCHO observations and uncertainty
542 weighted average for a time scale of about one month (Gonzalo et al., 2015; Zhu et al.,
543 2016) is needed to reduce the noise in daily OMI HCHO data. With improved satellite
544 HCHO data from TROPOMI, higher time resolution (e.g., weekly average) HCHO data
545 could be useful to estimate OA in the future.

546

547 **6.2 OA estimate over US**

548 The monthly average surface OA estimates over the US in August 2013 using SEAC⁴RS
549 lump-sum slope and intercept (see Table 2) with different η are shown in Fig. 6a and 6b.
550 Because BB regions in the US are not covered by smoke continuously during a period of
551 time and it is challenging for satellite retrieval to separate thick BB plumes and clouds
552 without information on the time and location of the burning, thick BB events (OMI UV
553 Aerosol Index (UVAI) > 1.6) (Torres et al., 2007) were excluded and shown as the blank
554 (white) grid cells in Fig. 6a and 6b. The same filter was also applied to aerosol extinction
555 and GEOS-Chem OA abundance. To evaluate the representative quality of the OA
556 estimate, OA estimate data were compared to the EPA IMPROVE ground sites corrected-
557 OA measurements over the US and SEARCH ground sites OA measurements in the SE
558 US (Sect. 2.2). The locations of IMPROVE and SEARCH sites are displayed in Fig. 6e
559 as small and large dots, respectively. The dot color represents the average OA mass
560 concentrations for August 2013.

561

562 Considering the uncertainties in satellite HCHO measurements, in using the campaign
563 lump-sum OA-HCHO relationship to represent spatial resolved OA, in HCHO vertical
564 profiles, and in ground IMPROVE network measurements, the correlation (correlation
565 coefficient $r = 0.56$) between the OA estimate and corrected IMPROVE network
566 measurements (Fig. 6f and 6g) is reasonably good and indicates that the OA estimate can
567 generally capture the variation of OA loading over the US. First, the correlation
568 coefficient between HCHO SAO retrievals and in situ measurements during SEAC⁴RS

569 was not high ($r = 0.24$) but this may be partly because they were not sampled at the same
570 time. The uncertainty in HCHO SAO data was likely less than 76%. Second, the
571 uncertainty in applying a campaign lump-sum OA-HCHO relationship to individual
572 spatial resolved satellite HCHO data to estimate OA induced an uncertainty of 41%
573 according to the correlation coefficient of OA-HCHO in the field campaign. Third, η in
574 the Fig. 6a OA estimate was from GEOS-Chem v9-02 output for the specific month
575 August, 2013. η in the Fig. 6b OA estimate was from GEOS-Chem v9-01-03
576 climatology, the same as satellite data a priori profiles. The good correlations of OA
577 estimates with IMPROVE OA indicate that OA estimates are not very sensitive to η from
578 different model versions. The largest difference between the two OA estimates is their
579 concentrations over East Texas. There are no IMPROVE OA measurements in the East
580 Texas to evaluate which works better. Fourth, the uncertainties in IMPROVE OA
581 measurements, such as using a constant correction factor to correct the partial
582 evaporation across all SE US sites, and the spatially dependent OA/OC ratio (Tsigaridis
583 et al., 2014), may also have contributed to the discrepancies between the OA estimate and
584 EPA IMPROVE sites OA. Therefore, higher quality of satellite HCHO data and refining
585 OA-HCHO relationships will help improve our OA estimate products. These combined
586 with a spatially resolved IMPROVE OA correction factor and OA/OC ratios will help
587 improve the correlation coefficients between OA estimates and IMPROVE OA.

588

589 The linear correlation between the OA estimate and IMPROVE OA measurements
590 yielded a slope of 0.62 or 0.60, indicating that the OA estimate underestimated OA. First,
591 the different data collection time for satellite data, in situ measurements and ground

592 observations could contribute to the bias. Satellite HCHO data were measured in mid-
593 day, in situ airborne OA and HCHO were measured during the daytime and IMPROVE
594 network organic carbon was collected day and night. Because ground OA in the SE US
595 were observed to have little diurnal variation (Xu et al., 2015; Hu et al., 2015), the
596 different sampling time of ground and airborne OA probably does not have a significant
597 impact on the comparison of OA estimate and IMPROVE OA. Surface HCHO has
598 evident diurnal profiles with the highest concentrations around the mid-day (Kaiser et al.,
599 2016), which could add uncertainties to OA estimate when using inconsistent time ranges
600 of satellite HCHO data measured in the mid-day and in situ airborne OA-HCHO
601 relationships measured in the daytime. The SEAC⁴RS HCHO concentrations were
602 converted to 1:30 pm concentrations according to the average HCHO diurnal profile from
603 the Southern Oxidant and Aerosol Study (SOAS) (Kaiser et al., 2016). The OA-HCHO
604 relationship with HCHO converted to 1:30 pm yielded a slope of 5% lower than the
605 original OA-HCHO relationship. Second, the potential uncertainty ($\pm 30\%$) in OA/OC
606 ratio could also contribute to the systematic difference because we used OA/OC of 2.1
607 and studies (e.g., Pye et al., 2017; Canagaratna et al., 2015) showed that the OA/OC can
608 range from 1.4 to 2.8. Third, the potential underestimation of HCHO from satellite
609 retrieval (by -37%) (Zhu et al., 2016) compared to SEAC⁴RS may be one of the most
610 important reasons that cause the systematic difference (low slope) between the OA
611 estimate and IMPROVE OA according to Eq. (1). Satellite HCHO data corrected by the
612 low bias (by -37%) (Zhu et al., 2016) will increase our slopes of 0.60-0.62 to be close to
613 the unity.
614

615 SEARCH OA data were also used to compare to the OA estimate. The correlation was
616 good for August 2013. Although the SEARCH network OA measurements have better
617 accuracy, the number of SEARCH sites is limited (5 sites). The correlation of OA
618 estimate and SEARCH OA varied dramatically 2008-2013 (Fig. S1). GEOS-Chem OA
619 did not correlate with SEARCH OA except for the year 2013 (Fig. S1). As the
620 IMPROVE network has more sites and spatial coverage, we used IMPROVE network
621 data as ground OA measurements for comparison in the remainder of the discussion.

622

623 **6.3 Comparison to aerosol extinction from AOD**

624 To further evaluate the method of using satellite HCHO to derive an OA surface estimate,
625 satellite aerosol measurements were used to approximate surface OA extinction for
626 comparison. Satellite measurements of AOD were converted to surface extinction (see
627 Sec. 2.6). Studies showed that OA were a dominant component of aerosol mass and
628 extinction during SEAC⁴RS (Kim et al., 2015; Wagner et al., 2015) and the fractions of
629 OA were relatively constant (interdecile 62-74%) (Wagner et al., 2015). Therefore AOD
630 variation is expected to generally reflect the OA variation during SEAC⁴RS. Satellite
631 measurements from MISR can provide more aerosol property information to apportion
632 total AOD to AOD of a subset of aerosols with small to medium size and round shape,
633 which can better capture OA, when AOD is above 0.15 to 0.2 (Kahn and Gaitley, 2015;
634 personal communication with R. Kahn, 2018). Because MISR cannot distinguish OA and
635 other submicron aerosol components (e.g., sulfate and nitrate) and would cut off low
636 AOD data which accounted for near half of the data over US, we used total AOD to
637 derive extinction for our comparison. The AOD-derived extinction map is shown in Fig.

638 6(c), and the scatter plot of AOD-derived extinction and EPA corrected OA is displayed
639 in Fig. 6(h). The same filter of high AI was also applied to AOD-derived extinction to
640 remove BB plumes. Generally, the derived aerosol extinction had a correlation with
641 IMPROVE OA, but the correlation was not as good as for the OA estimate with
642 IMPROVE OA. The high surface aerosol extinctions ($> 150 \text{ Mm}^{-1}$) (outliers in the
643 scatter plot) were located in the SE US and therefore were not due to potential
644 contribution of dust and nitrate altering the shape of vertical profiles outside of the SE
645 US. This indicates that the OA estimate derived from HCHO may be better than AOD at
646 representing the concentrations of OA, even for the regions where AOD is dominated by
647 OA (Xu et al., 2015).

648

649 **6.4 Comparison to GEOS-Chem OA**

650 Surface OA over the US from a GEOS-Chem simulation for August 2013 is shown in
651 Fig. 6(d), and the scatter plot of GEOS-Chem OA with IMPROVE OA is in Fig. 6(i).
652 Although HCHO vertical profiles from GEOS-Chem were used in OA estimate, the
653 GEOS-Chem simulation had a coarser resolution than OA estimate. To be comparable to
654 the OA estimate, the scatter plot Fig. 6(i) used GEOS-Chem results for the grid squares
655 that overlapped with individual IMPROVE sites. Compared to the OA estimate, GEOS-
656 Chem OA had a similar correlation coefficient with IMPROVE OA. Although the
657 GEOS-Chem OA plot appeared more scattered, there were many GEOS-Chem data
658 points close to zero when IMPROVE OA was low, making the overall correlation
659 coefficient similar to that for the OA estimate. GEOS-Chem under predicted IMPROVE

660 OA more with a slope of 0.57 compared to the OA estimate. This is consistent with
661 underprediction of anthropogenic OA in Marais et al. (2016).

662

663 **6.5 OA estimate with different OA-HCHO relationships**

664 OA were estimated with different OA-HCHO relationships for 4 cases (Table 2). LUMP-
665 SUM was using the non-BB SEAC⁴RS campaign lump-sum relationship, the same as
666 shown in Fig. 6; ISOP-NO_x was using non-BB SEAC⁴RS NO₂ and isoprene dependent
667 relationship; URBAN was using CalNex for large urban cities and SEAC⁴RS lump-sum
668 for other US regions; and COMBINE was using CalNex for large urban cities and NO₂
669 and isoprene dependent non-BB SEAC⁴RS for other US regions. The OA estimates from
670 the 4 cases (Table 2) were compared to IMPROVE OA and the correlation coefficients
671 are shown in Fig. 7. In general, OA estimate results from the four cases were similar.

672

673 The details about how to implement chemical factors dependent OA estimates for the
674 four cases are also provided in Table 2. Including the NO₂-isoprene-dependent OA-
675 HCHO relationship (ISOP-NO_x case) showed a similar (or slightly worse) correlation
676 between the OA estimate and IMPROVE OA. OMI NO₂ column observations were used
677 to represent surface NO₂ levels and surface isoprene emissions from MEGAN were used
678 to represent surface isoprene concentrations, assuming that NO₂ column observations
679 reflect surface NO₂ distributions and isoprene emissions reflect the concentrations of
680 isoprene due to its short lifetime (~1 hr). The detailed implementation is provided in the
681 notes in Table 2. As the in situ data showed a moderate NO₂-isoprene-dependent OA-
682 HCHO relationship, we attributed this to the locations of IMPROVE site at rural regions,

683 the uncertainty in IMPROVE network measurements, the uncertainty in isoprene
684 emissions from MEGAN, or factors (e.g., source-dependent OA-HCHO) that also need to
685 be taken into account when determining the specific OA-HCHO relationship. Satellite
686 OMI NO₂ data (at 1 : 30 pm) were used to represent NO₂ levels, big cities were defined
687 as NO₂ > 4 × 10¹⁵ molec cm⁻², and the CalNex in situ OA-HCHO relationship was
688 applied for big cities. It turned out that only 1 IMPROVE site (San Gabriel, SAGA1) near
689 LA was affected by high NO₂ and led to the insignificant change in URBAN compared to
690 LUMP-SUM. This is not unexpected because IMPROVE sites are in rural regions. The
691 OA estimate in SAGA1 decreased from 1.88 μg m⁻³ from LUMP-SUM to 0.17 μg m⁻³ in
692 URBAN while the measured OA in IMPROVE SAGA1 was 1.52 μg m⁻³. This may infer
693 that CalNex is not very consistent with SEAC⁴RS due to different sampling instruments,
694 strategies and seasons. Lowering the NO₂ threshold when defining big cities did not help
695 improve the agreement either.

696

697 Because separating large urban areas and other regions and applying a simple chemical
698 regime dependent in situ OA-HCHO relationship did not improve the agreement between
699 the OA estimate and IMPROVE OA, we used the lump-sum OA-HCHO relationship to
700 derive the OA estimate (shown in Fig. 6). SEAC⁴RS and DC3 only had a few low altitude
701 data in the Midwest and did not cover the Northeast US. The measured OA-HCHO
702 relationship in the Midwest did not show significant difference from the SE US. The
703 scatter plots (Fig. 6f and 6g) of OA estimates and IMPROVE OA do not show outliers
704 for the Northeast and Midwest. This indicates that using the SEAC⁴RS lump-sum OA-
705 HCHO relationship can reasonably capture regions outside of the SE US.

706

707 **6.6 Temporal variation of the agreement between OA estimate and IMPROVE OA**

708 Besides August 2013 (see Fig. 6), the correlations between the OA estimate and
709 IMPROVE OA for the summer months June-July-August 2008-2013 were also examined
710 and shown in Fig. 7. Generally, the correlation coefficients between the OA estimate and
711 IMPROVE OA were >0.5 for summer months of the years investigated. The correlation
712 coefficients were generally higher in June compared to July and August. The lower
713 average temperature in June might be related to the higher correlation coefficients.
714 IMPROVE network aerosol samples were transported at ambient temperature in a truck
715 and more organic vapors likely evaporated at higher temperature. The different
716 temperatures and distances from IMPROVE sites to the laboratory may lead to
717 inhomogeneous evaporation among the samples and result in lower correlation
718 coefficients. Although higher temperatures in July and August may also lead to more BB,
719 average aerosol index over the US was not higher in July (mean: 0.35) and August
720 (mean: 0.36) compared to June (mean: 0.39) for these years. The underlying cause for the
721 lowest correlation coefficients in July and August 2012 is not clear and may be related to
722 the severe drought in 2012 (Seco et al., 2015). The correlation coefficients were also low
723 for the linear regressions (not shown) of IMPROVE OA with both GEOS-Chem OA and
724 AOD-derived extinction. Because the lowest correlation coefficients were consistently
725 observed for multiple OA-related products and not just the OA estimate, we attributed
726 this to uncertainties in the IMPROVE OA measurements or some unknown bias shared
727 by the satellite HCHO, GEOS-Chem OA, and satellite AOD.

728

729 **6.7 South Korea OA estimate**

730 We attempted to estimate an OA estimate for South Korea, using airborne in situ
731 measurements of OA and HCHO from the KORUS-AQ field campaign (Aknan and
732 Chen, 2017) and SAO OMI HCHO measurements. The National Institute of
733 Environmental Research (NIER) ground sites OC measurements during KORUS-AQ
734 over South Korea could be used to validate the OA estimate. However, OMI HCHO
735 measurements were below the detection limit (Zhu et al., 2016) in May 2016. Also, there
736 were no OMI data available in June 2016 when airborne measurements and ground sites
737 OC measurements were available during KORUS-AQ. Because an OA estimate for South
738 Korea could not be well retrieved and validated, it was not presented in this study.
739 Although an OA estimate for South Korea could not be retrieved in the current study, the
740 consistency in the dependence of OA-HCHO relationships on chemical factors (e.g.,
741 emission sources, NO_x, and altitudes) provides important information for potential
742 application of chemical factors dependent OA-HCHO relationships to the geographical
743 domain beyond the continental US, especially with improved satellite HCHO data from
744 Tropospheric Monitoring Instrument (TROPOMI).

745

746 **7 Limitations of the OA estimate and future work**

747 Because the OA estimate is based on satellite HCHO data, the detection limit of satellite
748 HCHO data affects the quality of the OA estimate. Currently, due to the limited
749 sensitivity of OMI for HCHO, the OA estimate is valid only when high levels of HCHO
750 are present, such as during summer time and near large HCHO sources. With the new
751 TROPOMI satellite instrument and future missions TEMPO and GEMS, satellite HCHO

752 measurements will have higher spatial and temporal resolutions and lower detection
753 limits. These higher quality satellite HCHO measurements will improve the quality and
754 spatial and temporal coverage of our OA estimate.

755

756 Because the OA estimate uses the relationship of in situ HCHO and OA measurements,
757 the coverage of in situ aircraft field campaigns will impact the OA estimate quality.
758 Currently, in situ airborne measurements of OA and HCHO focus on the continental US.
759 Extending measurements to regions such as Africa BB, South America, and East Asia,
760 where HCHO and OA have high concentrations, will increase the spatial coverage of the
761 OA estimate product. Ground site measurements of OA with consistent quality control in
762 those regions will also be important for validating the OA estimate.

763

764 Improvement of satellite HCHO retrieval during the BB cases will also improve OA
765 estimate quality. BB cases with high UV aerosol index over the US were excluded in the
766 current OA estimate. With improvement in the satellite retrieval of HCHO, we may be
767 able to estimate OA during BB cases over the US. Upcoming field campaigns such as the
768 Fire Influence on Regional and Global Environments Experiment - Air Quality (FIREX-
769 AQ) will provide opportunities to improve the OA estimate in BB cases in the US.

770

771 This OA estimate method has limitations in remote regions far away from HCHO
772 sources. Because the lifetimes of HCHO (1-3 hours) and OA (1 week) are different, the
773 slopes and intercepts between HCHO and OA are expected to change when air masses
774 are aged (e.g., in remote regions). HCHO is close to being in steady-state with production

775 rates roughly equal to loss rates while OA is not in steady-state with a lifetime of a week.
776 Therefore, OA can be accumulated relative to HCHO when air masses are aged. OA vs.
777 HCHO from SEAC⁴RS and KORUS-AQ field campaigns, color-coded with altitude as an
778 indicator of air mass age, are plotted in Fig. S2 (a) and (b), respectively. A relative
779 depletion of HCHO at high altitudes was observed due to its shorter lifetime. This also
780 suggests that, at remote regions far away from the sources, the ratios of OA and HCHO
781 could be much higher and the relationship between OA and HCHO derived near the
782 sources may no longer apply. On the other hand, the lifetime of 1-3 hrs for HCHO does
783 not imply that the OA estimate only work within this timescale. HCHO is formed from
784 oxidation of transported gas phase VOCs, including the oxidation products of the primary
785 emitted VOCs, as well as of the slower reacting VOCs (e.g., Ethane and Benzene). Most
786 gas-to-particle oxidation processes that might produce HCHO can last up to 1-2 days
787 (Palm et al., 2018). Fig. S3 shows the ratios of OA and HCHO did not change
788 significantly downwind for the Rim Fire plume for about 1 day of aging, which was
789 determined by the distance from the source and the wind speed. A lower photolysis rate
790 of HCHO in the plume can also contribute to this. However, we do not expect the
791 relationship of OA and HCHO to remain past 1-2 boundary layer ventilation cycles (Palm
792 et al., 2018). Although OA-HCHO relationships depend on air mass age, it does not
793 largely affect our study for monthly average surface OA over continental US because our
794 OA estimates showed reasonably good agreement with ground sites IMPROVE OA
795 measurements. This also indicates that SOA are enhanced near the source regions
796 statistically. Nault et al. (2018) also showed the production of HCHO and SOA are
797 similar and plateau around 0.5 – 1 photochemical day. So, in the near field of emissions

798 and chemistry, the productions of these two species are similar; however, outside of near
799 field of emissions and rapid chemistry, the long lifetime of OA vs the steady state of
800 HCHO would start controlling the slopes and correlations.

801

802 **8 Summary**

803 We have developed a satellite-based estimate of the surface OA concentration (“OA
804 estimate”) based on in situ observations. This estimate is based on the empirical
805 relationships of in-situ OA and HCHO for several regions. OA and HCHO share VOC
806 sources with different yields and lifetimes. Using surface OA and HCHO linear
807 regression slopes and intercepts we can relate surface HCHO to OA. To estimate the
808 surface HCHO concentration from satellite HCHO column, we used a vertical
809 distribution factor η from either climatology satellite data a priori profiles or updated
810 model run for specific period, which is largely determined by boundary layer height and
811 surface emissions and found to reasonably retrieve surface HCHO from column HCHO.

812

813 The OA estimate over the continental US generally correlated well with EPA IMPROVE
814 network OA measurements corrected for partial evaporation, with a biased low slope of
815 0.62 or 0.60, mostly due to underestimation of HCHO concentrations from the OMI
816 HCHO retrieval. The good correlations are not only for the time during SEAC⁴RS but
817 also for most summer months over several years (2008-2013) investigated. Compared to
818 aerosol extinction derived from AOD, the OA estimate had slightly higher correlation
819 coefficients with IMPROVE OA. GEOS-Chem can predict OA with a similar correlation
820 coefficient with IMPROVE OA compared to the OA estimate when GEOS-Chem was

821 intensively validated with in situ measurements for SE US. Better satellite HCHO data
822 from TROPOMI and future TEMPO and GEMS and extending spatiotemporal coverage
823 of in situ measurements will improve the quality and coverage of the OA estimate.

824

825 **Author Contribution:**

826 JL performed the analysis and wrote the paper. TFH directed the research topic and
827 discussed the analysis with JL. TFH, GMW, JSC, AF and CW provided in situ HCHO
828 measurements. JLJ, PCJ, and BAN provided in situ OA measurements. EAM provided
829 GEOS-Chem model results. GGA and KC provided satellite HCHO data. HTJ provided
830 MODIS AOD data. TBR provided in situ NO₂ measurements. AW provided in situ
831 isoprene and acetonitrile measurements. GMW, TFH, JSC, JLJ, BAN, PCJ, EAM, and
832 GGA provided constructive comments to help improve the paper. All authors had
833 reviewed and edited the paper.

834

835 **Acknowledgements:**

836 JL, TFH, GMW, and JSC were supported by NASA grant NNH15ZDA001N and
837 NNH10ZDA001N. BAN, PCJ, and JLJ were supported by NASA grant NNX15AT96G
838 and 80NSSC18K0630. AW and PTR-MS measurements during DC3, SEAC⁴RS and
839 KORUS-AQ were supported by the Austrian Federal Ministry for Transport, Innovation
840 and Technology (bmvit) through the Austrian Space Applications Programme (ASAP) of
841 the Austrian Research Promotion Agency (FFG). The PTR-MS instrument team (P.
842 Eichler, L. Kaser, T. Mikoviny, M. Müller) is acknowledged for their field support. We
843 thank E. Edgerton for providing the SEARCH network data.

844 References:

- 845 Aknan, A. and Chen, G.: KORUS-AQ DC-8 Aircraft Dataset, available at: [https://www-](https://www-air.larc.nasa.gov/cgi-bin/ArcView/korusaq)
846 [air.larc.nasa.gov/cgi-bin/ArcView/korusaq](https://www-air.larc.nasa.gov/cgi-bin/ArcView/korusaq), last access: 3 February 2017.
847
- 848 Anderson, D. C., Loughner, C. P., Diskin, G., Weinheimer, A., Canty, T. P., Salawitch, R. J.,
849 Worden, H. M., Fried, A., Mikoviny, T., Wisthaler, A., and Dickerson, R. R.: Measured and
850 modeled CO and NO_y in DISCOVER-AQ: An evaluation of emissions and chemistry over the
851 eastern US, *Atmos Environ*, 96, 78-87, 10.1016/j.atmosenv.2014.07.004, 2014.
852
- 853 Attwood, A. R., Washenfelder, R. A., Brock, C. A., Hu, W., Baumann, K., Campuzano-Jost, P.,
854 Day, D. A., Edgerton, E. S., Murphy, D. M., Palm, B. B., McComiskey, A., Wagner, N. L., de
855 Sa, S. S., Ortega, A., Martin, S. T., Jimenez, J. L., and Brown, S. S.: Trends in sulfate and
856 organic aerosol mass in the Southeast U.S.: Impact on aerosol optical depth and radiative
857 forcing, *Geophys Res Lett*, 41, 7701-7709, 10.1002/2014gl061669, 2014.
858
- 859 Bahreini, R., Middlebrook, A. M., de Gouw, J. A., Warneke, C., Trainer, M., Brock, C. A., Stark,
860 H., Brown, S. S., Dube, W. P., Gilman, J. B., Hall, K., Holloway, J. S., Kuster, W. C., Perring,
861 A. E., Prevot, A. S. H., Schwarz, J. P., Spackman, J. R., Szidat, S., Wagner, N. L., Weber, R. J.,
862 Zotter, P., and Parrish, D. D.: Gasoline emissions dominate over diesel in formation of secondary
863 organic aerosol mass, *Geophys Res Lett*, 39, Artn L06805
864 10.1029/2011gl050718, 2012.
865
- 866 Baker, A. K., Beyersdorf, A. J., Doezema, L. A., Katzenstein, A., Meinardi, S., Simpson, I. J.,
867 Blake, D. R., and Rowland, F. S.: Measurements of nonmethane hydrocarbons in 28 United
868 States cities, *Atmos Environ*, 42, 170-182, 10.1016/j.atmosenv.2007.09.007, 2008.
869
- 870 Barth, M. C., Cantrell, C. A., Brune, W. H., Rutledge, S. A., Crawford, J. H., Huntrieser, H.,
871 Carey, L. D., MacGorman, D., Weisman, M., Pickering, K. E., Bruning, E., Anderson, B., Apel,
872 E., Biggerstaff, M., Campos, T., Campuzano-Jost, P., Cohen, R., Crouse, J., Day, D. A., Diskin,
873 G., Flocke, F., Fried, A., Garland, C., Heikes, B., Honomichl, S., Hornbrook, R., Huey, L. G.,
874 Jimenez, J. L., Lang, T., Lichtenstern, M., Mikoviny, T., Nault, B., O'Sullivan, D., Pan, L. L.,
875 Peischl, J., Pollack, I., Richter, D., Riemer, D., Ryerson, T., Schlager, H., St Clair, J., Walega, J.,
876 Weibring, P., Weinheimer, A., Wennberg, P., Wisthaler, A., Wooldridge, P. J., and Ziegler, C.:
877 The Deep Convective Clouds and Chemistry (Dc3) Field Campaign, *B Am Meteorol Soc*, 96,
878 1281-1309, 10.1175/Bams-D-13-00290.1, 2015.
879
- 880 Bianchi, F., Barmet, P., Stirnweis, L. El Haddad, I., Platt, S.M., Saurer, M., Lötscher, C.,
881 Siegwolf, R., Bigi, A., Hoyle, C.R., DeCarlo, P.F., Slowik, J.G., Prévôt, A.S.H., Baltensperger,
882 U., and Dommen. Contribution of methane to aerosol carbon mass. *Atmospheric Environment*,
883 141, 41-47, doi: 10.1016/j.atmosenv.2016.06.036, 2016.
884
- 885 Canagaratna, M. R., Jayne, J. T., Jimenez, J. L., Allan, J. D., Alfarra, M. R., Zhang, Q., Onasch,
886 T. B., Drewnick, F., Coe, H., Middlebrook, A., Delia, A., Williams, L. R., Trimborn, A. M.,
887 Northway, M. J., DeCarlo, P. F., Kolb, C. E., Davidovits, P., and Worsnop, D. R.: Chemical and
888 microphysical characterization of ambient aerosols with the aerodyne aerosol mass spectrometer,
889 *Mass Spectrom Rev*, 26, 185-222, 10.1002/mas.20115, 2007.

890
891 Canagaratna, M. R., Jimenez, J. L., Kroll, J. H., Chen, Q., Kessler, S. H., Massoli, P.,
892 Hildebrandt Ruiz, L., Fortner, E., Williams, L. R., Wilson, K. R., Surratt, J. D., Donahue, N. M.,
893 Jayne, J. T., and Worsnop, D. R.: Elemental ratio measurements of organic compounds using
894 aerosol mass spectrometry: characterization, improved calibration, and implications, *Atmos*
895 *Chem Phys*, 15, 253-272, <https://doi.org/10.5194/acp-15-253-2015>, 2015.
896
897 Carslaw, K. S., Lee, L. A., Reddington, C. L., Pringle, K. J., Rap, A., Forster, P. M., Mann, G.
898 W., Spracklen, D. V., Woodhouse, M. T., Regayre, L. A., and Pierce, J. R.: Large contribution of
899 natural aerosols to uncertainty in indirect forcing, *Nature*, 503, 67-+, [10.1038/nature12674](https://doi.org/10.1038/nature12674), 2013.
900
901 Cazorla, M., Wolfe, G. M., Bailey, S. A., Swanson, A. K., Arkinson, H. L., and Hanisco, T. F.: A
902 new airborne laser-induced fluorescence instrument for in situ detection of formaldehyde
903 throughout the troposphere and lower stratosphere, *Atmos Meas Tech*, 8, 541-552, [10.5194/amt-](https://doi.org/10.5194/amt-8-541-2015)
904 [8-541-2015](https://doi.org/10.5194/amt-8-541-2015), 2015.
905
906 Cubison, M. J., Ortega, A. M., Hayes, P. L., Farmer, D. K., Day, D., Lechner, M. J., Brune, W.
907 H., Apel, E., Diskin, G. S., Fisher, J. A., Fuelberg, H. E., Hecobian, A., Knapp, D. J., Mikoviny,
908 T., Riemer, D., Sachse, G. W., Sessions, W., Weber, R. J., Weinheimer, A. J., Wisthaler, A., and
909 Jimenez, J. L.: Effects of aging on organic aerosol from open biomass burning smoke in aircraft
910 and laboratory studies, *Atmos. Chem. Phys.*, 11, 12049-12064, [https://doi.org/10.5194/acp-11-](https://doi.org/10.5194/acp-11-12049-2011)
911 [12049-2011](https://doi.org/10.5194/acp-11-12049-2011), 2011.
912
913 Day, D. A., Wooldridge, P. J., Dillon, M. B., Thornton, J. A., and Cohen, R. C.: A thermal
914 dissociation laser-induced fluorescence instrument for in situ detection of NO₂, peroxy nitrates,
915 alkyl nitrates, and HNO₃, *J Geophys Res-Atmos*, 107, Artn 4046
916 [10.1029/2001jd000779](https://doi.org/10.1029/2001jd000779), 2002.
917
918 de Vries, M. J. M. P., Beirle, S., Hormann, C., Kaiser, J. W., Stammes, P., Tilstra, L. G.,
919 Tuinder, O. N. E., and Wagner, T.: A global aerosol classification algorithm incorporating
920 multiple satellite data sets of aerosol and trace gas abundances, *Atmos Chem Phys*, 15, 10597-
921 10618, [10.5194/acp-15-10597-2015](https://doi.org/10.5194/acp-15-10597-2015), 2015.
922
923 DeCarlo, P. F., Kimmel, J. R., Trimborn, A., Northway, M. J., Jayne, J. T., Aiken, A. C., Gonin,
924 M., Fuhrer, K., Horvath, T., Docherty, K. S., Worsnop, D. R., and Jimenez, J. L.: Field-
925 deployable, high-resolution, time-of-flight aerosol mass spectrometer, *Anal Chem*, 78, 8281-
926 8289, [10.1021/ac061249n](https://doi.org/10.1021/ac061249n), 2006.
927
928 DeCarlo, P. F., Ulbrich, I. M., Crouse, J., de Foy, B., Dunlea, E. J., Aiken, A. C., Knapp, D.,
929 Weinheimer, A. J., Campos, T., Wennberg, P. O., and Jimenez, J. L.: Investigation of the sources
930 and processing of organic aerosol over the Central Mexican Plateau from aircraft measurements
931 during MILAGRO, *Atmos. Chem. Phys.*, 10, 5257-5280, [https://doi.org/10.5194/acp-10-5257-](https://doi.org/10.5194/acp-10-5257-2010)
932 [2010](https://doi.org/10.5194/acp-10-5257-2010), 2010.
933
934 Dufour, G., Wittrock, F., Camredon, M., Beekmann, M., Richter, A., Aumont, B., Burrows, J.P.,
935 SCIAMACHY formaldehyde observations: constraint for isoprene emission estimates over

936 Europe? *Atmos Chem Phys*, 9,1647–1664, 2009.

937

938 Drewnick, F., Hings, S. S., DeCarlo, P., Jayne, J. T., Gonin, M., Fuhrer, K., Weimer, S.,
 939 Jimenez, J. L., Demerjian, K. L., Borrmann, S., and Worsnop, D. R.: A new time-of-flight
 940 aerosol mass spectrometer (TOF-AMS) - Instrument description and first field deployment,
 941 *Aerosol Sci Tech*, 39, 637-658, 10.1080/02786820500182040, 2005.

942

943 Dunlea, E. J., DeCarlo, P. F., Aiken, A. C., Kimmel, J. R., Peltier, R. E., Weber, R. J.,
 944 Tomlinson, J., Collins, D. R., Shinozuka, Y., McNaughton, C. S., Howell, S. G., Clarke, A. D.,
 945 Emmons, L. K., Apel, E. C., Pfister, G. G., van Donkelaar, A., Martin, R. V., Millet, D. B.,
 946 Heald, C. L., and Jimenez, J. L.: Evolution of Asian aerosols during transpacific transport in
 947 INTEX-B, *Atmos Chem Phys*, 9, 7257-7287, DOI 10.5194/acp-9-7257-2009, 2009.

948

949 Edgerton, E. S., Hartsell, B. E., Saylor, R. D., Jansen, J. J., Hansen, D. A., and Hidy, G. M.: The
 950 Southeastern Aerosol Research and Characterization Study, part 3: Continuous measurements of
 951 fine particulate matter mass and composition, *J Air Waste Manage*, 56, 1325-1341, Doi
 952 10.1080/10473289.2006.10464585, 2006.

953

954 Gelaro, R., McCarty, W., Suarez, M. J., Todling, R., Molod, A., Takacs, L., Randles, C. A.,
 955 Darmenov, A., Bosilovich, M. G., Reichle, R., Wargan, K., Coy, L., Cullather, R., Draper, C.,
 956 Akella, S., Buchard, V., Conaty, A., da Silva, A. M., Gu, W., Kim, G. K., Koster, R., Lucchesi,
 957 R., Merkova, D., Nielsen, J. E., Partyka, G., Pawson, S., Putman, W., Rienecker, M., Schubert,
 958 S. D., Sienkiewicz, M., and Zhao, B.: The Modern-Era Retrospective Analysis for Research and
 959 Applications, Version 2 (MERRA-2), *J Climate*, 30, 5419-5454, 10.1175/Jcli-D-16-0758.1,
 960 2017.

961

962 Giglio, L., Randerson, J. T., and van der Werf, G. R.: Analysis of daily, monthly, and
 963 annual burned area using the fourth-generation global fire emissions database (GFED4):
 964 *J. Geophys. Res.-Biogeo.*, 118, 317–328, <https://doi.org/10.1002/jgrg.20042>, 2013.

965

966 Gonzalez Abad, G. G., Liu, X., Chance, K., Wang, H., Kurosu, T. P., and Suleiman, R.: Updated
 967 Smithsonian Astrophysical Observatory Ozone Monitoring Instrument (SAO OMI)
 968 formaldehyde retrieval, *Atmos Meas Tech*, 8, 19-32, 10.5194/amt-8-19-2015, 2015.

969

970 Guenther, A., Karl, T., Harley, P., Wiedinmyer, C., Palmer, P. I., and Geron, C.: Estimates of
 971 global terrestrial isoprene emissions using MEGAN (Model of Emissions of Gases and Aerosols
 972 from Nature), *Atmos Chem Phys*, 6, 3181-3210, DOI 10.5194/acp-6-3181-2006, 2006.

973

974 Hand, J. L., Schichtel, B. A., Malm, W. C., and Frank, N. H.: Spatial and Temporal Trends in
 975 PM_{2.5} Organic and Elemental Carbon across the United States, *Adv Meteorol*, Artn 367674,
 976 10.1155/2013/367674, 2013.

977

978 Hand, J. L., Schichtel, B. A., Malm, W. C., Pitchford, M., and Frank, N. H.: Spatial and seasonal
 979 patterns in urban influence on regional concentrations of speciated aerosols across the United
 980 States, *J Geophys Res-Atmos*, 119, 12832-12849, 10.1002/2014jd022328, 2014.

981

982 Harvard-Smithsonia Center for Astrophysics, OMI HCHO data product description:

983 <https://www.cfa.harvard.edu/atmosphere/Instruments/OMI/PGEReleases/READMEs/OMHCHO>
984 [README_v3.0.pdf](#), last accessed: 22 January, 2019.
985
986 Hayes, P. L., Carlton, A. G., Baker, K. R., Ahmadov, R., Washenfelder, R. A., Alvarez, S.,
987 Rappenglück, B., Gilman, J. B., Kuster, W. C., de Gouw, J. A., Zotter, P., Prévôt, A. S. H.,
988 Szidat, S., Kleindienst, T. E., Offenberg, J. H., Ma, P. K., and Jimenez, J. L.: Modeling the
989 formation and aging of secondary organic aerosols in Los Angeles during CalNex 2010, *Atmos.*
990 *Chem. Phys.*, 15, 5773-5801, <https://doi.org/10.5194/acp-15-5773-2015>, 2015.
991
992 Hayes, P. L., Ortega, A. M., Cubison, M. J., Froyd, K. D., Zhao, Y., Cliff, S. S., Hu, W. W.,
993 Toohey, D. W., Flynn, J. H., Lefer, B. L., Grossberg, N., Alvarez, S., Rappenglueck, B., Taylor,
994 J. W., Allan, J. D., Holloway, J. S., Gilman, J. B., Kuster, W. C., De Gouw, J. A., Massoli, P.,
995 Zhang, X., Liu, J., Weber, R. J., Corrigan, A. L., Russell, L. M., Isaacman, G., Worton, D. R.,
996 Kreisberg, N. M., Goldstein, A. H., Thalman, R., Waxman, E. M., Volkamer, R., Lin, Y. H.,
997 Surratt, J. D., Kleindienst, T. E., Offenberg, J. H., Dusanter, S., Griffith, S., Stevens, P. S.,
998 Brioude, J., Angevine, W. M., and Jimenez, J. L.: Organic aerosol composition and sources in
999 Pasadena, California, during the 2010 CalNex campaign, *J Geophys Res-Atmos*, 118, 9233-
1000 9257, 10.1002/jgrd.50530, 2013.
1001
1002 Heald, C. L., Coe, H., Jimenez, J. L., Weber, R. J., Bahreini, R., Middlebrook, A. M., Russell, L.
1003 M., Jolleys, M., Fu, T. M., Allan, J. D., Bower, K. N., Capes, G., Crosier, J., Morgan, W. T.,
1004 Robinson, N. H., Williams, P. I., Cubison, M. J., DeCarlo, P. F., and Dunlea, E. J.: Exploring the
1005 vertical profile of atmospheric organic aerosol: comparing 17 aircraft field campaigns with a
1006 global model, *Atmos Chem Phys*, 11, 12673-12696, 10.5194/acp-11-12673-2011, 2011.
1007
1008 Heald, C. L., Goldstein, A. H., Allan, J. D., Aiken, A. C., Apel, E., Atlas, E. L., Baker, A. K.,
1009 Bates, T. S., Beyersdorf, A. J., Blake, D. R., Campos, T., Coe, H., Crouse, J. D., DeCarlo, P. F.,
1010 de Gouw, J. A., Dunlea, E. J., Flocke, F. M., Fried, A., Goldan, P., Griffin, R. J., Herndon, S. C.,
1011 Holloway, J. S., Holzinger, R., Jimenez, J. L., Junkermann, W., Kuster, W. C., Lewis, A. C.,
1012 Meinardi, S., Millet, D. B., Onasch, T., Polidori, A., Quinn, P. K., Riemer, D. D., Roberts, J. M.,
1013 Salcedo, D., Sive, B., Swanson, A. L., Talbot, R., Warneke, C., Weber, R. J., Weibring, P.,
1014 Wennberg, P. O., Worsnop, D. R., Wittig, A. E., Zhang, R., Zheng, J., and Zheng, W.: Total
1015 observed organic carbon (TOOC) in the atmosphere: a synthesis of North American
1016 observations, *Atmos Chem Phys*, 8, 2007-2025, 10.5194/acp-8-2007-2008, 2008.
1017
1018 Hidy, G. M., Blanchard, C. L., Baumann, K., Edgerton, E., Tanenbaum, S., Shaw, S., Knipping,
1019 E., Tombach, I., Jansen, J., and Walters, J.: Chemical climatology of the southeastern United
1020 States, 1999-2013, *Atmos Chem Phys*, 14, 11893-11914, 10.5194/acp-14-11893-2014, 2014.
1021
1022 Hodzic, A., and Jimenez, J. L.: Modeling anthropogenically controlled secondary organic
1023 aerosols in a megacity: a simplified framework for global and climate models, *Geosci Model*
1024 *Dev*, 4, 901-917, 10.5194/gmd-4-901-2011, 2011.
1025
1026 Hu, W. W., Campuzano-Jost, P., Palm, B. B., Day, D. A., Ortega, A. M., Hayes, P. L.,
1027 Krechmer, J. E., Chen, Q., Kuwata, M., Liu, Y. J., de Sá, S. S., McKinney, K., Martin, S. T., Hu,
1028 M., Budisulistiorini, S. H., Riva, M., Surratt, J. D., St. Clair, J. M., Isaacman-Van Wertz, G.,

1029 Yee, L. D., Goldstein, A. H., Carbone, S., Brito, J., Artaxo, P., de Gouw, J. A., Koss, A.,
1030 Wisthaler, A., Mikoviny, T., Karl, T., Kaser, L., Jud, W., Hansel, A., Docherty, K. S., Alexander,
1031 M. L., Robinson, N. H., Coe, H., Allan, J. D., Canagaratna, M. R., Paulot, F., and Jimenez, J. L.:
1032 Characterization of a real-time tracer for isoprene epoxydiols-derived secondary organic aerosol
1033 (IEPOX-SOA) from aerosol mass spectrometer measurements, *Atmos. Chem. Phys.*, 15, 11807-
1034 11833, <https://doi.org/10.5194/acp-15-11807-2015>, 2015.
1035
1036 Hudson, P. K., Murphy, D. M., Cziczo, D. J., Thomson, D. S., de Gouw, J. A., Warneke, C.,
1037 Holloway, J., Jost, J. R., and Hubler, G.: Biomass-burning particle measurements: Characteristic
1038 composition and chemical processing, *J Geophys Res-Atmos*, 109, ArtD23s27
1039 10.1029/2003jd004398, 2004.
1040
1041 Jimenez, J. L., Canagaratna, M. R., Donahue, N. M., Prevot, A. S. H., Zhang, Q., Kroll, J. H.,
1042 DeCarlo, P. F., Allan, J. D., Coe, H., Ng, N. L., Aiken, A. C., Docherty, K. S., Ulbrich, I. M.,
1043 Grieshop, A. P., Robinson, A. L., Duplissy, J., Smith, J. D., Wilson, K. R., Lanz, V. A., Hueglin,
1044 C., Sun, Y. L., Tian, J., Laaksonen, A., Raatikainen, T., Rautiainen, J., Vaattovaara, P., Ehn, M.,
1045 Kulmala, M., Tomlinson, J. M., Collins, D. R., Cubison, M. J., Dunlea, E. J., Huffman, J. A.,
1046 Onasch, T. B., Alfarra, M. R., Williams, P. I., Bower, K., Kondo, Y., Schneider, J., Drewnick, F.,
1047 Borrmann, S., Weimer, S., Demerjian, K., Salcedo, D., Cottrell, L., Griffin, R., Takami, A.,
1048 Miyoshi, T., Hatakeyama, S., Shimono, A., Sun, J. Y., Zhang, Y. M., Dzepina, K., Kimmel, J.
1049 R., Sueper, D., Jayne, J. T., Herndon, S. C., Trimborn, A. M., Williams, L. R., Wood, E. C.,
1050 Middlebrook, A. M., Kolb, C. E., Baltensperger, U., and Worsnop, D. R.: Evolution of Organic
1051 Aerosols in the Atmosphere, *Science*, 326, 1525-1529, 10.1126/science.1180353, 2009.
1052
1053 Jimenez, J. L., Canagaratna, M. R., Drewnick, F., Allan, J. D., Alfarra, M. R., Middlebrook, A.
1054 M., Slowik, J. G., Zhang, Q., Coe, H., Jayne, J. T., and Worsnop, D. R.: Comment on "The
1055 effects of molecular weight and thermal decomposition on the sensitivity of a thermal desorption
1056 aerosol mass spectrometer", *Aerosol Sci Tech*, 50, I-Xv, 10.1080/02786826.2016.1205728,
1057 2016.
1058
1059 Kahn, R. A., and Gaitley, B. J.: An analysis of global aerosol type as retrieved by MISR, *J*
1060 *Geophys Res-Atmos*, 120, 4248-4281, 10.1002/2015jd023322, 2015.
1061
1062 Kaiser, J., Jacob, D. J., Zhu, L., Travis, K. R., Fisher, J. A., Abad, G. G., Zhang, L., Zhang, X.
1063 S., Fried, A., Crouse, J. D., St Clair, J. M., and Wisthaler, A.: High-resolution inversion of OMI
1064 formaldehyde columns to quantify isoprene emission on ecosystem-relevant scales: application
1065 to the southeast US, *Atmos Chem Phys*, 18, 5483-5497, 10.5194/acp-18-5483-2018, 2018.
1066
1067 Kaiser, J., Skog, K. M., Baumann, K., Bertman, S. B., Brown, S. B., Brune, W. H., Crouse, J.
1068 D., de Gouw, J. A., Edgerton, E. S., Feiner, P. A., Goldstein, A. H., Koss, A., Misztal, P. K.,
1069 Nguyen, T. B., Olson, K. F., St Clair, J. M., Teng, A. P., Toma, S., Wennberg, P. O., Wild, R. J.,
1070 Zhang, L., and Keutsch, F. N.: Speciation of OH reactivity above the canopy of an isoprene-
1071 dominated forest, *Atmos Chem Phys*, 16, 9349-9359, 2016.
1072
1073 Kiehl, J. T., and Briegleb, B. P.: The Relative Roles of Sulfate Aerosols and Greenhouse Gases
1074 in Climate Forcing, *Science*, 260, 311-314, DOI 10.1126/science.260.5106.311, 1993.

1075
1076 Kim, P. S., Jacob, D. J., Fisher, J. A., Travis, K., Yu, K., Zhu, L., Yantosca, R. M., Sulprizio, M.
1077 P., Jimenez, J. L., Campuzano-Jost, P., Froyd, K. D., Liao, J., Hair, J. W., Fenn, M. A., Butler, C.
1078 F., Wagner, N. L., Gordon, T. D., Welti, A., Wennberg, P. O., Crounse, J. D., St Clair, J. M.,
1079 Teng, A. P., Millet, D. B., Schwarz, J. P., Markovic, M. Z., and Perring, A. E.: Sources,
1080 seasonality, and trends of southeast US aerosol: an integrated analysis of surface, aircraft, and
1081 satellite observations with the GEOS-Chem chemical transport model, *Atmos Chem Phys*, 15,
1082 10411-10433, 10.5194/acp-15-10411-2015, 2015.
1083
1084 Kröll, J. H., Ng, N. L., Murphy, S. M., Flagan, R. C., and Seinfeld, J. H.: Secondary organic
1085 aerosol formation from isoprene photooxidation, *Environ Sci Technol*, 40, 1869-1877,
1086 10.1021/es0524301, 2006.
1087
1088 Lamarque, J. F., Bond, T. C., Eyring, V., Granier, C., Heil, A., Klimont, Z., Lee, D., Liousse, C.,
1089 Mieville, A., Owen, B., Schultz, M. G., Shindell, D., Smith, S. J., Stehfest, E., Van Aardenne, J.,
1090 Cooper, O. R., Kainuma, M., Mahowald, N., McConnell, J. R., Naik, V., Riahi, K., and van
1091 Vuuren, D. P.: Historical (1850-2000) gridded anthropogenic and biomass burning emissions of
1092 reactive gases and aerosols: methodology and application, *Atmos Chem Phys*, 10, 7017-7039,
1093 10.5194/acp-10-7017-2010, 2010.
1094
1095 Lamsal, L. N., Krotkov, N. A., Celarier, E. A., Swartz, W. H., Pickering, K. E., Bucsela, E. J.,
1096 Gleason, J. F., Martin, R. V., Philip, S., Irie, H., Cede, A., Herman, J., Weinheimer, A.,
1097 Szykman, J. J., and Knepp, T. N.: Evaluation of OMI operational standard NO₂ column
1098 retrievals using in situ and surface-based NO₂ observations, *Atmos Chem Phys*, 14, 11587-
1099 11609, 10.5194/acp-14-11587-2014, 2014.
1100
1101 Lee, A., Goldstein, A. H., Kröll, J. H., Ng, N. L., Varutbangkul, V., Flagan, R. C., Seinfeld, J.
1102 H., Gas-phase products and secondary aerosol yields from the photooxidation of 16 different
1103 terpenes, *J Geophys Res- Atmos*, 111, D17, <https://doi.org/10.1029/2006JD007050>, 2006.
1104
1105 Lee-Taylor, J., Hodzic, A., Madronich, S., Aumont, B., Camredon, M., and Valorso, R.:
1106 Multiday production of condensing organic aerosol mass in urban and forest outflow, *Atmos*
1107 *Chem Phys*, 15, 595-615, 10.5194/acp-15-595-2015, 2015.
1108
1109 Levelt, P. F., Van den Oord, G. H. J., Dobber, M. R., Malkki, A., Visser, H., de Vries, J.,
1110 Stammes, P., Lundell, J. O. V., and Saari, H.: The Ozone Monitoring Instrument, *Ieee T Geosci*
1111 *Remote*, 44, 1093-1101, 10.1109/Tgrs.2006.872333, 2006.
1112
1113 Levy, R. C., Munchak, L. A., Mattoo, S., Patadia, F., Remer, L. A., and Holz, R. E.: Towards a
1114 long-term global aerosol optical depth record: applying a consistent aerosol retrieval algorithm to
1115 MODIS and VIIRS-observed reflectance, *Atmos Meas Tech*, 8, 4083-4110, 10.5194/amt-8-
1116 4083-2015, 2015.
1117
1118 Liu, X. X., Huey, L. G., Yokelson, R. J., Selimovic, V., Simpson, I. J., Muller, M., Jimenez, J.
1119 L., Campuzano-Jost, P., Beyersdorf, A. J., Blake, D. R., Butterfield, Z., Choi, Y., Crounse, J. D.,
1120 Day, D. A., Diskin, G. S., Dubey, M. K., Fortner, E., Hanisco, T. F., Hu, W. W., King, L. E.,

1121 Kleinman, L., Meinardi, S., Mikoviny, T., Onasch, T. B., Palm, B. B., Peischl, J., Pollack, I. B.,
 1122 Ryerson, T. B., Sachse, G. W., Sedlacek, A. J., Shilling, J. E., Springston, S., St Clair, J. M.,
 1123 Tanner, D. J., Teng, A. P., Wennberg, P. O., Wisthaler, A., and Wolfe, G. M.: Airborne
 1124 measurements of western US wildfire emissions: Comparison with prescribed burning and air
 1125 quality implications, *J Geophys Res-Atmos*, 122, 6108-6129, 10.1002/2016jd026315, 2017.
 1126
 1127 Malm, W. C., Sisler, J. F., Huffman, D., Eldred, R. A., and Cahill, T. A.: Spatial and Seasonal
 1128 Trends in Particle Concentration and Optical Extinction in the United-States, *J Geophys Res-*
 1129 *Atmos*, 99, 1347-1370, Doi 10.1029/93jd02916, 1994.
 1130
 1131 Malm, W. C., Schichtel, B. A., Hand, J. L., and Collett, J. L.: Concurrent Temporal and Spatial
 1132 Trends in Sulfate and Organic Mass Concentrations Measured in the IMPROVE Monitoring
 1133 Program, *J Geophys Res-Atmos*, 122, 10341-10355, 10.1002/2017jd026865, 2017.
 1134
 1135 Marais, E. A., Jacob, D. J., Jimenez, J. L., Campuzano-Jost, P., Day, D. A., Hu, W., Krechmer,
 1136 J., Zhu, L., Kim, P. S., Miller, C. C., Fisher, J. A., Travis, K., Yu, K., Hanisco, T. F., Wolfe, G.
 1137 M., Arkinson, H. L., Pye, H. O. T., Froyd, K. D., Liao, J., and McNeill, V. F.: Aqueous-phase
 1138 mechanism for secondary organic aerosol formation from isoprene: application to the southeast
 1139 United States and co-benefit of SO₂ emission controls, *Atmos Chem Phys*, 16, 1603-1618,
 1140 10.5194/acp-16-1603-2016, 2016.
 1141
 1142 Marais, E. A., Jacob, D. J., Turner, J. R., and Mickley, L. J.: Evidence of 1991-2013 decrease of
 1143 biogenic secondary organic aerosol in response to SO₂ emission controls, *Environ Res Lett*, 12,
 1144 ARTN 054018
 1145 10.1088/1748-9326/aa69c8, 2017.
 1146
 1147 McDonald, B. C., de Gouw, J. A., Gilman, J. B., Jathar, S. H., Akherati, A., Cappa, C. D.,
 1148 Jimenez, J. L., Lee-Taylor, J., Hayes, P. L., McKeen, S. A., Cui, Y. Y., Kim, S. W., Gentner, D.
 1149 R., Isaacman-VanWertz, G., Goldstein, A. H., Harley, R. A., Frost, G. J., Roberts, J. M.,
 1150 Ryerson, T. B., and Trainer, M.: Volatile chemical products emerging as largest petrochemical
 1151 source of urban organic emissions, *Science*, 359, 760-764, ARTN aaq0524
 1152 10.1126/science.aaq0524, 2018.
 1153
 1154 Millet, D. B., Jacob, D. J., Boersma, K. F., Fu, T. M., Kurosu, T. P., Chance, K., Heald, C. L.,
 1155 and Guenther, A.: Spatial distribution of isoprene emissions from North America derived from
 1156 formaldehyde column measurements by the OMI satellite sensor, *J Geophys Res-Atmos*, 113,
 1157 Artn D02307
 1158 10.1029/2007jd008950, 2008.
 1159
 1160 Murphy, D. M., Cziczo, D. J., Froyd, K. D., Hudson, P. K., Matthew, B. M., Middlebrook, A.
 1161 M., Peltier, R. E., Sullivan, A., Thomson, D. S., and Weber, R. J.: Single-particle mass
 1162 spectrometry of tropospheric aerosol particles, *J Geophys Res-Atmos*, 111, Artn D23s32
 1163 10.1029/2006jd007340, 2006.
 1164
 1165 Na, K., Kim, Y. P., and Moon, K. C.: Seasonal variation of the C-2-C-9 hydrocarbons
 1166 concentrations and compositions emitted from motor vehicles in a Seoul tunnel, *Atmos Environ*,

1167 36, 1969-1978, Pii S1352-2310(02)00149-8
1168 Doi 10.1016/S1352-2310(02)00149-8, 2002.
1169
1170 Na, K., Moon, K. C., and Kim, Y. P.: Source contribution to aromatic VOC concentration and
1171 ozone formation potential in the atmosphere of Seoul, *Atmos Environ*, 39, 5517-5524,
1172 10.1016/j.atmosenv.2005.06.005, 2005.
1173
1174 NASA OMI NO₂ data archive, data product OMI-Aura_L3-OMNO2d,
1175 [hbps://disc.sci.gsfc.nasa.gov](https://disc.sci.gsfc.nasa.gov), last accessed: 4 January, 2017.
1176
1177 NASA MODIS AOD data archive, data product MYD04_L2, [hbps://ladsweb.nascom.nasa.gov/](https://ladsweb.nascom.nasa.gov/),
1178 last accessed: 20 October, 2019.
1179
1180 Nault, B. A., Campuzano-Jost, P., Day, D. A., Schroder, J. C., Anderson, B., Beyersdorf, A. J.,
1181 Blake, D. R., Brune, W. H., Choi, Y., Corr, C. A., de Gouw, J. A., Dibb, J., DiGangi, J. P.,
1182 Diskin, G. S., Fried, A., Huey, L. G., Kim, M. J., Knote, C. J., Lamb, K. D., Lee, T., Park, T.,
1183 Pusede, S. E., Scheuer, E., Thornhill, K. L., Woo, J.-H., and Jimenez, J. L.: Secondary Organic
1184 Aerosol Production from Local Emissions Dominates the Organic Aerosol Budget over Seoul,
1185 South Korea, during KORUS-AQ, *Atmos. Chem. Phys.*, 18, 17769-17800,
1186 <https://doi.org/10.5194/acp-2018-838>, 2018.
1187
1188 Ng, N. L., Kroll, J. H., Chan, A. W. H., Chhabra, P. S., Flagan, R. C., and Seinfeld, J. H.:
1189 Secondary organic aerosol formation from m-xylene, toluene, and benzene, *Atmos Chem Phys*,
1190 7, 3909-3922, DOI 10.5194/acp-7-3909-2007, 2007.
1191
1192 Palm, B. B., de Sa, S. S., Day, D. A., Campuzano-Jost, P., Hu, W. W., Seco, R., Sjostedt, S. J.,
1193 Park, J. H., Guenther, A. B., Kim, S., Brito, J., Wurm, F., Artaxo, P., Thalman, R., Wang, J.,
1194 Yee, L. D., Wernis, R., Isaacman-VanWertz, G., Goldstein, A. H., Liu, Y. J., Springston, S. R.,
1195 Souza, R., Newburn, M. K., Alexander, M. L., Martin, S. T., and Jimenez, J. L.: Secondary
1196 organic aerosol formation from ambient air in an oxidation flow reactor in central Amazonia,
1197 *Atmos Chem Phys*, 18, 467-493, 10.5194/acp-18-467-2018, 2018.
1198
1199 Pope, C. A., Burnett, R. T., Thun, M. J., Calle, E. E., Krewski, D., Ito, K., and Thurston, G. D.:
1200 Lung cancer, cardiopulmonary mortality, and long-term exposure to fine particulate air pollution,
1201 *Jama-J Am Med Assoc*, 287, 1132-1141, DOI 10.1001/jama.287.9.1132, 2002.
1202
1203 Pye, H. O. T., Chan, A. W. H., Barkley, M. P., and Seinfeld, J. H.: Global modeling of organic
1204 aerosol: the importance of reactive nitrogen (NO_x and NO₃), *Atmos Chem Phys*, 10, 11261-
1205 11276, 10.5194/acp-10-11261-2010, 2010.
1206
1207 Pye, H. O. T., Murphy, B. N., Xu, L., Ng, N. L., Carlton, A. G., Guo, H., Weber, R., Vasilakos,
1208 P., Appel, K. W., Budisulistiorini, S. H., Surratt, J. D., Nenes, A., Hu, W., Jimenez, J. L.,
1209 Isaacman-VanWertz, G., Misztal, P. K., and Goldstein, A. H.: On the implications of aerosol
1210 liquid water and phase separation for organic aerosol mass, *Atmos. Chem. Phys.*, 17, 343-369,
1211 <https://doi.org/10.5194/acp-17-343-2017>, 2017.
1212

1213 Richter, D., Weibring, P., Walega, J. G., Fried, A., Spuler, S. M., and Taubman, M. S.: Compact
1214 highly sensitive multi-species airborne mid-IR spectrometer, *Appl Phys B-Lasers O*, 119, 119-
1215 131, 10.1007/s00340-015-6038-8, 2015.

1216
1217 Ridley, D. A., Heald, C. L., Ridley, K. J., and Kroll, J. H.: Causes and consequences of
1218 decreasing atmospheric organic aerosol in the United States, *P Natl Acad Sci USA*, 115, 290-
1219 295, 10.1073/pnas.1700387115, 2018.

1220
1221 Robinson, A. L., Donahue, N. M., Shrivastava, M. K., Weitkamp, E. A., Sage, A. M., Grieshop,
1222 A. P., Lane, T. E., Pierce, J. R., and Pandis, S. N.: Rethinking organic aerosols: Semivolatile
1223 emissions and photochemical aging, *Science*, 315, 1259-1262, 10.1126/science.1133061, 2007.

1224 Ryerson, T. B., Andrews, A. E., Angevine, W. M., Bates, T. S., Brock, C. A., Cairns, B., Cohen,
1225 R. C., Cooper, O. R., de Gouw, J. A., Fehsenfeld, F. C., Ferrare, R. A., Fischer, M. L., Flagan, R.
1226 C., Goldstein, A. H., Hair, J. W., Hardesty, R. M., Hostetler, C. A., Jimenez, J. L., Langford, A.
1227 O., McCauley, E., McKeen, S. A., Molina, L. T., Nenes, A., Oltmans, S. J., Parrish, D. D.,
1228 Pederson, J. R., Pierce, R. B., Prather, K., Quinn, P. K., Seinfeld, J. H., Senff, C. J., Sorooshian,
1229 A., Stutz, J., Surratt, J. D., Trainer, M., Volkamer, R., Williams, E. J., and Wofsy, S. C.: The
1230 2010 California Research at the Nexus of Air Quality and Climate Change (CalNex) field study,
1231 *J Geophys Res-Atmos*, 118, 5830-5866, 10.1002/jgrd.50331, 2013.

1232
1233 Ryerson, T. B., Trainer, M., Holloway, J. S., Parrish, D. D., Huey, L. G., Sueper, D. T., Frost, G.
1234 J., Donnelly, S. G., Schauffler, S., Atlas, E. L., Kuster, W. C., Goldan, P. D., Hubler, G.,
1235 Meagher, J. F., and Fehsenfeld, F. C.: Observations of ozone formation in power plant plumes
1236 and implications for ozone control strategies, *Science*, 292, 719-723, DOI
1237 10.1126/science.1058113, 2001.

1238
1239 Seco, R., Karl, T., Guenther, A., Hosman, K. P., Pallardy, S. G., Gu, L. H., Geron, C., Harley, P.,
1240 and Kim, S.: Ecosystem-scale volatile organic compound fluxes during an extreme drought in a
1241 broadleaf temperate forest of the Missouri Ozarks (central USA), *Global Change Biol*, 21, 3657-
1242 3674, 10.1111/gcb.12980, 2015.

1243
1244 Schroder, J.C, P. Campuzano-Jost, D.A. Day, V. Shah, K. Larson, J.M. Sommers, A.P.
1245 Sullivan, T. Campos, J.M. Reeves, A. Hills, R. S. Hornbrook, N.J. Blake, E. Scheuer, H.
1246 Guo, D.L. Fibiger, E.E. McDuffie, P.L. Hayes, R.J. Weber, J.E. Dibb, E.C. Apel, L.
1247 Jaeglé, S.S. Brown, J.A. Thornton, J.L. Jimenez. Sources and Secondary Production of
1248 Organic Aerosols in the Northeastern US during WINTER. *J. Geophys. Res.-Atmos.*,
1249 123, <https://doi.org/10.1029/2018JD028475>, 2018.

1250
1251 Shrivastava, M., Cappa, C. D., Fan, J. W., Goldstein, A. H., Guenther, A. B., Jimenez, J. L.,
1252 Kuang, C., Laskin, A., Martin, S. T., Ng, N. L., Petaja, T., Pierce, J. R., Rasch, P. J., Roldin, P.,
1253 Seinfeld, J. H., Shilling, J., Smith, J. N., Thornton, J. A., Volkamer, R., Wang, J., Worsnop, D.
1254 R., Zaveri, R. A., Zelenyuk, A., and Zhang, Q.: Recent advances in understanding secondary
1255 organic aerosol: Implications for global climate forcing, *Rev Geophys*, 55, 509-559,
1256 10.1002/2016rg000540, 2017.

1257
1258 Solomon, P. A., Crumpler, D., Flanagan, J. B., Jayanty, R. K. M., Rickman, E. E., and McDade,

1259 C. E.: US National PM_{2.5} Chemical Speciation Monitoring Networks-CSN and IMPROVE:
1260 Description of networks, *J Air Waste Manage*, 64, 1410-1438, 10.1080/10962247.2014.956904,
1261 2014.
1262
1263 Stocker, T.F., D. Qin, G.-K. Plattner, M. Tignor, S.K. Allen, J. Boschung, A. Nauels, Y.
1264 Xia, V. Bex and P.M. Midgley (eds.), IPCC, 2013: *Climate Change 2013: The Physical
1265 Science Basis. Contribution of Working Group I to the Fifth Assessment Report of the
1266 Intergovernmental Panel on Climate Change*. Cambridge University Press, Cambridge,
1267 United Kingdom and New York, NY, USA, 1535 pp, doi:10.1017/CBO9781107415324.
1268
1269
1270 Taylor, K. E., and Penner, J. E.: Response of the Climate System to Atmospheric Aerosols and
1271 Greenhouse Gases, *Nature*, 369, 734-737, DOI 10.1038/369734a0, 1994.
1272
1273 Tong, D. Q., Lamsal, L., Pan, L., Ding, C., Kim, H., Lee, P., Chai, T. F., Pickering, K. E., and
1274 Stajner, I.: Long-term NO_x trends over large cities in the United States during the great
1275 recession: Comparison of satellite retrievals, ground observations, and emission inventories,
1276 *Atmos Environ*, 107, 70-84, 10.1016/j.atmosenv.2015.01.035, 2015.
1277
1278 Toon, O. B., Maring, H., Dibb, J., Ferrare, R., Jacob, D. J., Jensen, E. J., Luo, Z. J., Mace, G. G.,
1279 Pan, L. L., Pfister, L., Rosenlof, K. H., Redemann, J., Reid, J. S., Singh, H. B., Thompson, A.
1280 M., Yokelson, R., Minnis, P., Chen, G., Jucks, K. W., and Pszenny, A.: Planning,
1281 implementation, and scientific goals of the Studies of Emissions and Atmospheric Composition,
1282 Clouds and Climate Coupling by Regional Surveys (SEAC(4)RS) field mission, *J Geophys Res-
1283 Atmos*, 121, 4967-5009, 10.1002/2015jd024297, 2016.
1284
1285 Torres, O., Tanskanen, A., Veihelmann, B., Ahn, C., Braak, R., Bhartia, P. K., Veeffkind, P., and
1286 Levelt, P.: Aerosols and surface UV products from Ozone Monitoring Instrument observations:
1287 An overview, *J Geophys Res-Atmos*, 112, Artn D24s47
1288 10.1029/2007jd008809, 2007.
1289
1290 Travis, K. R., Jacob, D. J., Fisher, J. A., Kim, P. S., Marais, E. A., Zhu, L., Yu, K., Miller, C. C.,
1291 Yantosca, R. M., Sulprizio, M. P., Thompson, A. M., Wennberg, P. O., Crouse, J. D., St Clair,
1292 J. M., Cohen, R. C., Laughner, J. L., Dibb, J. E., Hall, S. R., Ullmann, K., Wolfe, G. M., Pollack,
1293 I. B., Peischl, J., Neuman, J. A., and Zhou, X. L.: Why do models overestimate surface ozone in
1294 the Southeast United States?, *Atmos Chem Phys*, 16, 13561-13577, 10.5194/acp-16-13561-2016,
1295 2016.
1296
1297 Tsigaridis, K., Daskalakis, N., Kanakidou, M., Adams, P. J., Artaxo, P., Bahadur, R., Balkanski,
1298 Y., Bauer, S. E., Bellouin, N., Benedetti, A., Bergman, T., Berntsen, T. K., Beukes, J. P., Bian,
1299 H., Carslaw, K. S., Chin, M., Curci, G., Diehl, T., Easter, R. C., Ghan, S. J., Gong, S. L., Hodzic,
1300 A., Hoyle, C. R., Iversen, T., Jathar, S., Jimenez, J. L., Kaiser, J. W., Kirkevag, A., Koch, D.,
1301 Kokkola, H., Lee, Y. H., Lin, G., Liu, X., Luo, G., Ma, X., Mann, G. W., Mihalopoulos, N.,
1302 Morcrette, J. J., Muller, J. F., Myhre, G., Myriokefalitakis, S., Ng, N. L., O'Donnell, D., Penner,
1303 J. E., Pozzoli, L., Pringle, K. J., Russell, L. M., Schulz, M., Sciare, J., Seland, O., Shindell, D. T.,
1304 Sillman, S., Skeie, R. B., Spracklen, D., Stavrou, T., Steenrod, S. D., Takemura, T., Tiitta, P.,

1305 Tilmes, S., Tost, H., van Noije, T., van Zyl, P. G., von Salzen, K., Yu, F., Wang, Z., Wang, Z.,
1306 Zaveri, R. A., Zhang, H., Zhang, K., Zhang, Q., and Zhang, X.: The AeroCom evaluation and
1307 intercomparison of organic aerosol in global models, *Atmos Chem Phys*, 14, 10845-10895,
1308 10.5194/acp-14-10845-2014, 2014.
1309
1310 Veefkind, J. P., Boersma, K. F., Wang, J., Kurosu, T. P., Krotkov, N., Chance, K., and Levelt, P.
1311 F.: Global satellite analysis of the relation between aerosols and short-lived trace gases, *Atmos*
1312 *Chem Phys*, 11, 1255-1267, 10.5194/acp-11-1255-2011, 2011.
1313
1314 Wagner, N. L., Brock, C. A., Angevine, W. M., Beyersdorf, A., Campuzano-Jost, P., Day, D., de
1315 Gouw, J. A., Diskin, G. S., Gordon, T. D., Graus, M. G., Holloway, J. S., Huey, G., Jimenez, J.
1316 L., Lack, D. A., Liao, J., Liu, X., Markovic, M. Z., Middlebrook, A. M., Mikoviny, T., Peischl,
1317 J., Perring, A. E., Richardson, M. S., Ryerson, T. B., Schwarz, J. P., Warneke, C., Welti, A.,
1318 Wisthaler, A., Ziemba, L. D., and Murphy, D. M.: In situ vertical profiles of aerosol extinction,
1319 mass, and composition over the southeast United States during SENEX and SEAC(4)RS:
1320 observations of a modest aerosol enhancement aloft, *Atmos Chem Phys*, 15, 7085-7102,
1321 10.5194/acp-15-7085-2015, 2015.
1322
1323 Walgraeve, C., Demeestere, K., Dewulf, J., Zimmermann, R., and Van Langenhove, H.:
1324 Oxygenated polycyclic aromatic hydrocarbons in atmospheric particulate matter: Molecular
1325 characterization and occurrence, *Atmos Environ*, 44, 1831-1846,
1326 10.1016/j.atmosenv.2009.12.004, 2010.
1327
1328 Warneke, C., de Gouw, J. A., Stohl, A., Cooper, O. R., Goldan, P. D., Kuster, W. C., Holloway,
1329 J. S., Williams, E. J., Lerner, B. M., McKeen, S. A., Trainer, M., Fehsenfeld, F. C., Atlas, E. L.,
1330 Donnelly, S. G., Stroud, V., Lueb, A., and Kato, S.: Biomass burning and anthropogenic sources
1331 of CO over New England in the summer 2004, *J Geophys Res-Atmos*, 111, Artn D23s15
1332 10.1029/2005jd006878, 2006.
1333
1334 Warneke, C., Veres, P., Holloway, J. S., Stutz, J., Tsai, C., Alvarez, S., Rappenglueck, B.,
1335 Fehsenfeld, F. C., Graus, M., Gilman, J. B., and de Gouw, J. A.: Airborne formaldehyde
1336 measurements using PTR-MS: calibration, humidity dependence, inter-comparison and initial
1337 results, *Atmos Meas Tech*, 4, 2345-2358, 10.5194/amt-4-2345-2011, 2011.
1338
1339 Weibring, P., Richter, D., Fried, A., Walega, J. G., and Dyroff, C.: Ultra-high-precision mid-IR
1340 spectrometer II: system description and spectroscopic performance, *Appl Phys B-Lasers O*, 85,
1341 207-218, 10.1007/s00340-006-2300-4, 2006.
1342
1343 Wisthaler A., Hansel A., Dickerson R. R., Crutzen P. J.: Organic trace gas measurements
1344 by PTR-MS during INDOEX 1999, *J Geophys Res-Atmos*, 107(D19), 8024, 2002.
1345
1346 Wolfe, G. M., Kaiser, J., Hanisco, T. F., Keutsch, F. N., de Gouw, J. A., Gilman, J. B., Graus,
1347 M., Hatch, C. D., Holloway, J., Horowitz, L. W., Lee, B. H., Lerner, B. M., Lopez-Hilifiker, F.,
1348 Mao, J., Marvin, M. R., Peischl, J., Pollack, I. B., Roberts, J. M., Ryerson, T. B., Thornton, J. A.,
1349 Veres, P. R., and Warneke, C.: Formaldehyde production from isoprene oxidation across NO_x
1350 regimes, *Atmos Chem Phys*, 16, 2597-2610, 10.5194/acp-16-2597-2016, 2016.

1351
1352 Worton, D.R., J.D. Surratt, B.W. Lafranchi, A.W.H. Chan, Y. Zhao, R. Weber, J. Park, J.B.
1353 Gilman, J. de Gouw, C. Park, G. Schade, M. Beaver, J. StClair, J. Crouse, P. Wennberg, G.
1354 Wolfe, S. Harrold, J. Thornton, D. K. Farmer, K.S. Docherty, Mi.J. Cubison, J.L. Jimenez, A.
1355 Frossard, L. Russell, K. Kristensen, M. Glasius, J. Mao, X. Ren, W.H. Brune, E. Browne, S.
1356 Pusede, R. Cohen, J.H. Seinfeld and A.H. Goldstein. Observational Insights into Aerosol
1357 Formation from Isoprene. *Environmental Science & Technology*, 47, 11403-11413,
1358 doi:10.1021/es4011064, 2013.
1359
1360 Xu, L., Middlebrook, A. M., Liao, J., de Gouw, J. A., Guo, H. Y., Weber, R. J., Nenes, A.,
1361 Lopez-Hilfiker, F. D., Lee, B. H., Thornton, J. A., Brock, C. A., Neuman, J. A., Nowak, J. B.,
1362 Pollack, I. B., Welti, A., Graus, M., Warneke, C., and Ng, N. L.: Enhanced formation of
1363 isoprene-derived organic aerosol in sulfur-rich power plant plumes during Southeast Nexus, *J*
1364 *Geophys Res-Atmos*, 121, 11137-11153, 10.1002/2016jd025156, 2016.
1365
1366 Xu, L., Suresh, S., Guo, H., Weber, R. J., and Ng, N. L.: Aerosol characterization over the
1367 southeastern United States using high-resolution aerosol mass spectrometry: spatial and seasonal
1368 variation of aerosol composition and sources with a focus on organic nitrates, *Atmos Chem Phys*,
1369 15, 7307-7336, 10.5194/acp-15-7307-2015, 2015.
1370
1371 Yu, K. R., Jacob, D. J., Fisher, J. A., Kim, P. S., Marais, E. A., Miller, C. C., Travis, K. R., Zhu,
1372 L., Yantosca, R. M., Sulprizio, M. P., Cohen, R. C., Dibb, J. E., Fried, A., Mikoviny, T.,
1373 Ryerson, T. B., Wennberg, P. O., and Wisthaler, A.: Sensitivity to grid resolution in the ability of
1374 a chemical transport model to simulate observed oxidant chemistry under high-isoprene
1375 conditions, *Atmos Chem Phys*, 16, 4369-4378, 10.5194/acp-16-4369-2016, 2016.
1376
1377 Zhang, H. F., Yee, L. D., Lee, B. H., Curtis, M. P., Worton, D. R., Isaacman-VanWertz, G.,
1378 Offenberg, J. H., Lewandowski, M., Kleindienst, T. E., Beaver, M. R., Holder, A. L., Lonneman,
1379 W. A., Docherty, K. S., Jaoui, M., Pye, H. O. T., Hu, W. W., Day, D. A., Campuzano-Jost, P.,
1380 Jimenez, J. L., Guo, H. Y., Weber, R. J., de Gouw, J., Koss, A. R., Edgerton, E. S., Brune, W.,
1381 Mohr, C., Lopez-Hilfiker, F. D., Lutz, A., Kreisberg, N. M., Spielman, S. R., Hering, S. V.,
1382 Wilson, K. R., Thornton, J. A., and Goldstein, A. H.: Monoterpenes are the largest source of
1383 summertime organic aerosol in the southeastern United States, *P Natl Acad Sci USA*, 115, 2038-
1384 2043, 10.1073/pnas.1717513115, 2018.
1385
1386 Zhu, L., Jacob, D. J., Keutsch, F. N., Mickley, L. J., Scheffe, R., Strum, M., Abad, G. G.,
1387 Chance, K., Yang, K., Rappengluck, B., Millet, D. B., Baasandorj, M., Jaegle, L., and Shah, V.:
1388 Formaldehyde (HCHO) As a Hazardous Air Pollutant: Mapping Surface Air Concentrations
1389 from Satellite and Inferring Cancer Risks in the United States, *Environ Sci Technol*, 51, 5650-
1390 5657, 10.1021/acs.est.7b01356, 2017.
1391
1392 Zhu, L., Jacob, D. J., Kim, P. S., Fisher, J. A., Yu, K., Travis, K. R., Mickley, L. J., Yantosca, R.
1393 M., Sulprizio, M. P., De Smedt, I., Abad, G. G., Chance, K., Li, C., Ferrare, R., Fried, A., Hair, J.
1394 W., Hanisco, T. F., Richter, D., Scarino, A. J., Walega, J., Weibring, P., and Wolfe, G. M.:
1395 Observing atmospheric formaldehyde (HCHO) from space: validation and intercomparison of six
1396 retrievals from four satellites (OMI, GOME2A, GOME2B, OMPS) with SEAC(4)RS aircraft

1397 observations over the southeast US, *Atmos Chem Phys*, 16, 13477-13490, 10.5194/acp-16-
1398 13477-2016, 2016.
1399
1400 Ziemann, P.J., and Atkinson, R. Kinetics, products, and mechanisms of secondary organic
1401 aerosol formation. *Chem. Soc. Rev.*, 41, 6582-6605, doi: 10.1039/C2CS35122F, 2012.
1402

1403 Tables

1404

1405 Table 1. Linear regression parameters for OA vs. HCHO at low altitudes (<1 km)

1406

	US (SEAC ⁴ RS)	US (DC3)	US (CalNex)	South Korea (KORUS- AQ)	Wild Fires (SEAC ⁴ RS)	Agricultural Fires (SEAC ⁴ RS)	SEAC ⁴ RS Low NO ₂ and Isoprene	SEAC ⁴ RS high NO ₂ and Isoprene
In situ measurements OA v.s. HCHO								
Slope ^a	1.93±0.07	1.30± 0.10	1.34±0.02	2.75±0.05	25.08±0.30	3.22±0.37	2.39±0.09	1.45±0.19
Slope ^b (×10 ⁻¹¹)	9.61± 0.34	6.49± 0.49	6.66±0.09	13.7 ± 0.25	125.05 ± 1.49	16.04 ± 1.85	11.9±0.43	7.25±0.96
Intercept ^c	0.34±0.32	1.10±0.30	-0.90±0.06	1.36±0.22	-6.85±2.80	10.41±5.82	-1.14±0.37	1.14±1.22
Correlation coefficient r	0.59	0.76	0.88	0.70	0.97	0.85	0.64	0.45
Number of points (1 min avg)	1506	134	1772	3425	515	32	1138	226
GEOS- Chem model sampled along the flight track OA v.s. HCHO								
Slope ^a	1.25±0.03			1.39±0.05	0.48±0.05			
Slope (×10 ⁻¹¹)	6.21± 0.14			6.95± 0.23	2.37± 0.22			
Intercept	-1.32 ±0.11			1.88 ± 0.07	0.12±0.03			
Correlation Coefficient r	0.76			0.43	0.53			

1407

1408

1409

1410

1411

1412

^a The unit of the slope is g g⁻¹.

^b The unit of the slope is pg molec⁻¹.

^c The unit of the intercept is µg m⁻³.

The uncertainties are one standard deviation.

1413 Table 2. Cases to estimate OA surface concentrations, based on the choice of slope and

1414 intercept from a linear regression relationship between OA and HCHO data found in

1415 Table 1.

1416

LUMP-SUM ^a	Using non-BB SEAC ⁴ RS relationship to represent all continental US
ISOP-NO _x ^b	Using NO ₂ and isoprene dependent non-BB SEAC ⁴ RS relationship for all continental US
URBAN	Using the CalNex LA Basin relationship for large urban cites and the non-biomass burning SEAC ⁴ RS relationship for other US regions
COMBINE ^b	Using the CalNex LA Basin relationship for large urban cites and the NO ₂ and isoprene dependent non-BB SEAC ⁴ RS relationship for other US regions

1417

1418 ^aSEAC⁴RS was chosen to represent all continental US because it had the largest horizontal and vertical

1419 coverage.

1420 ^b In cases ISOP-NO_x and COMBINE, when the product of NO₂ column (Sect. 2.3) and surface isoprene

1421 emission rate (Sect. 2.4) was above threshold of 5×10²⁷ molec cm⁻² atom C cm⁻² s⁻¹, the slope and intercept

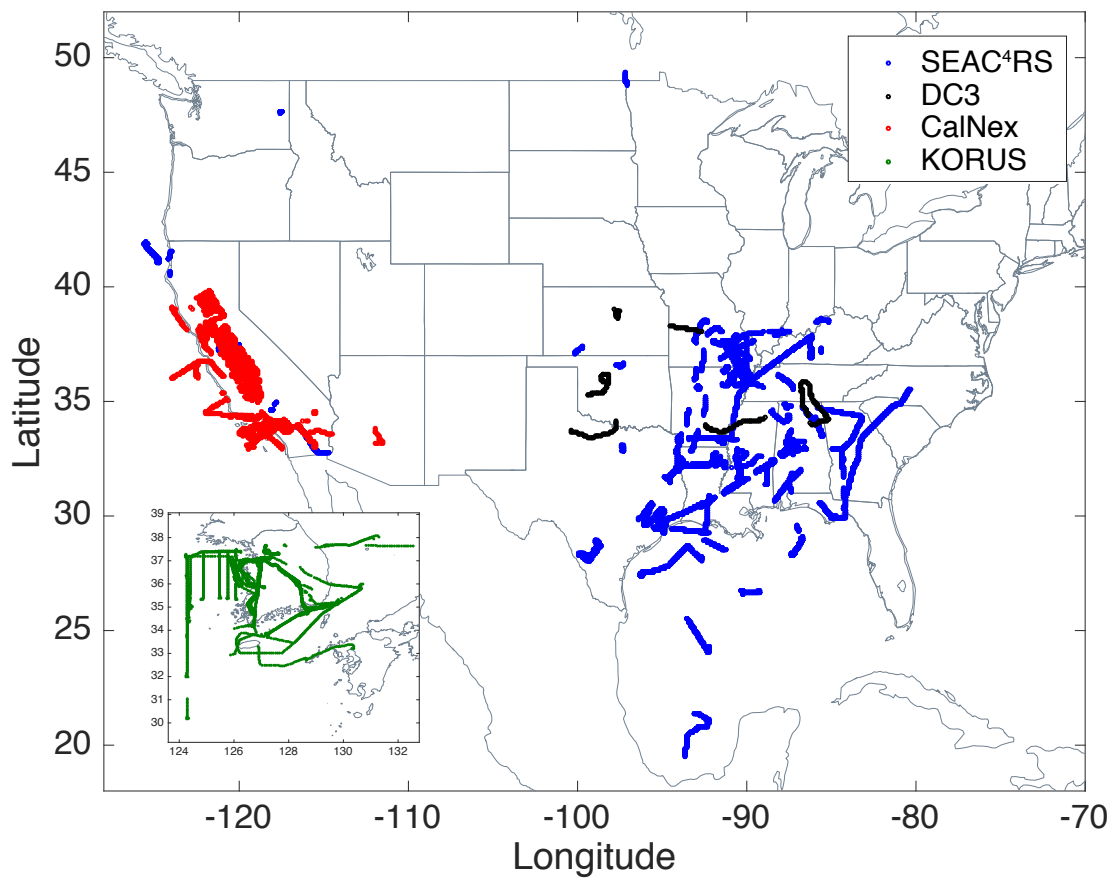
1422 from SEAC⁴RS high isoprene and NO₂ conditions were used. When the NO₂ column–isoprene emission

1423 product was below that threshold, the slope and intercept from SEAC⁴RS low isoprene and NO₂ conditions
1424 were used. Threshold of “Isoprene × NO₂” was determined by its mean value over SE US (83° - 96° W and
1425 32° - 35°N). Large urban cities were categorized with high NO₂ vertical columns ($>4 \times 10^{15}$ molec cm⁻²)
1426 (Tong et al., 2015) based on the satellite NO₂ levels over LA. Isoprene emissions instead of concentrations
1427 were used because global models use isoprene emission inventory to simulate isoprene concentrations and
1428 isoprene emission inventory is easier to access. Since isoprene has a short-lifetime of up to a few hours
1429 (Guenther et al., 2006), the emissions have a similar spatiotemporal distribution as the concentrations.
1430

1431

1432 Figures

1433



1434

1435

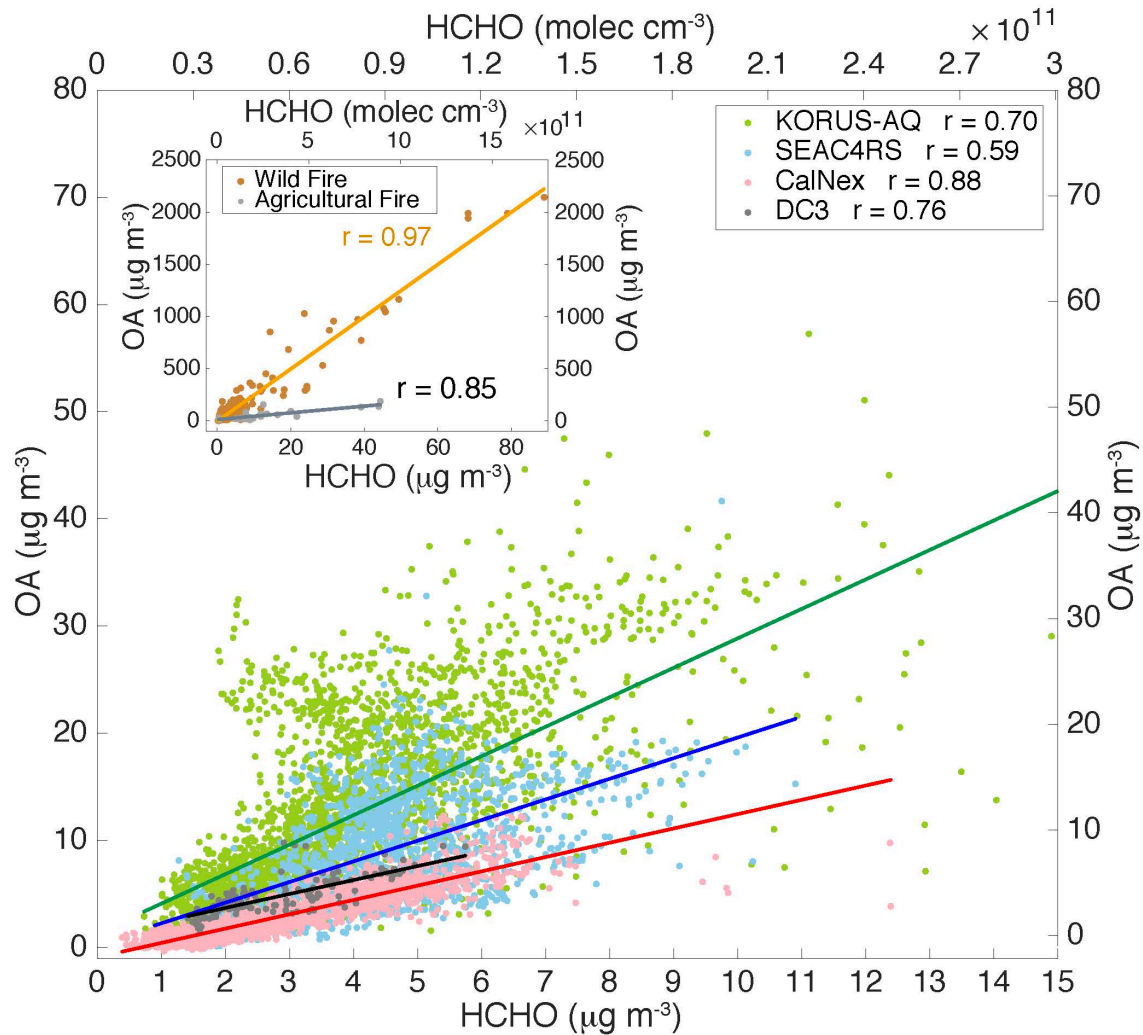
1436 Figure 1. Flight tracks of airborne field campaigns SEAC⁴RS (blue), DC3 (black),
1437 CalNex (red) and KORUS-AQ (green) with altitudes (< 1 km), of which in situ OA and
1438 HCHO measurements were used.

1439

1440

1441

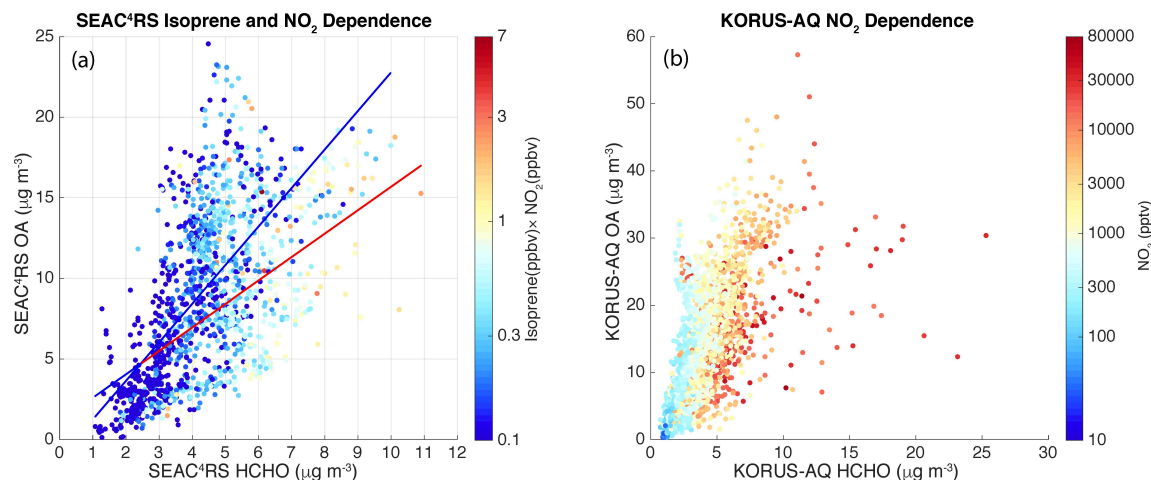
1442



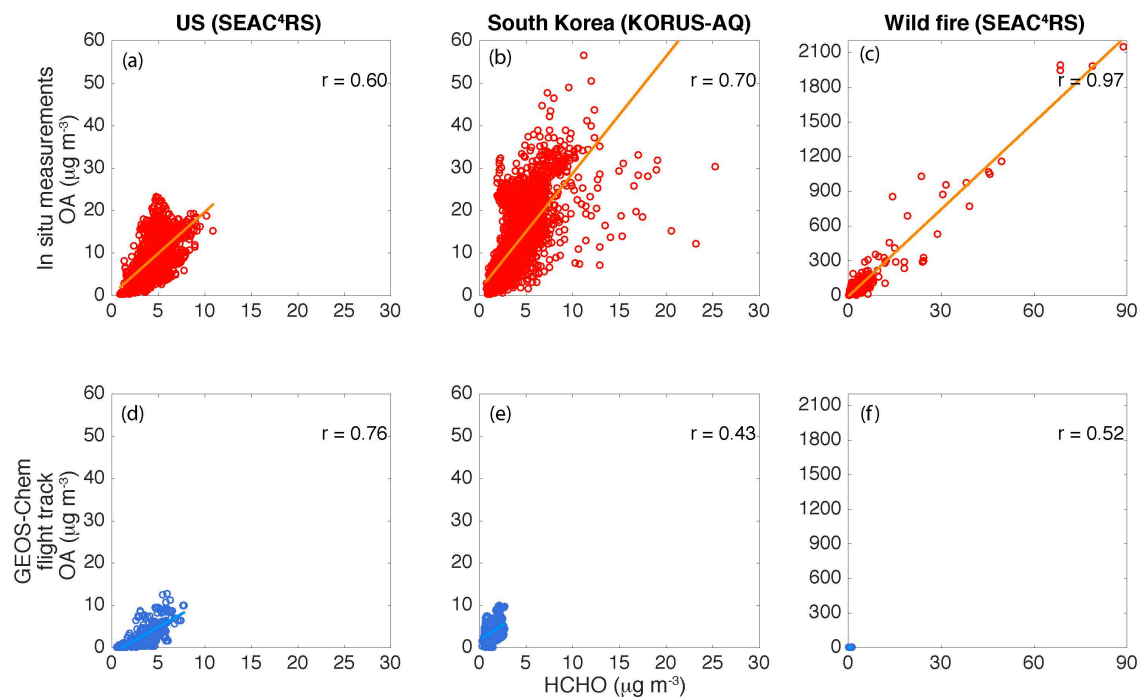
1443
 1444
 1445
 1446
 1447
 1448
 1449
 1450
 1451
 1452
 1453
 1454
 1455
 1456

Figure 2

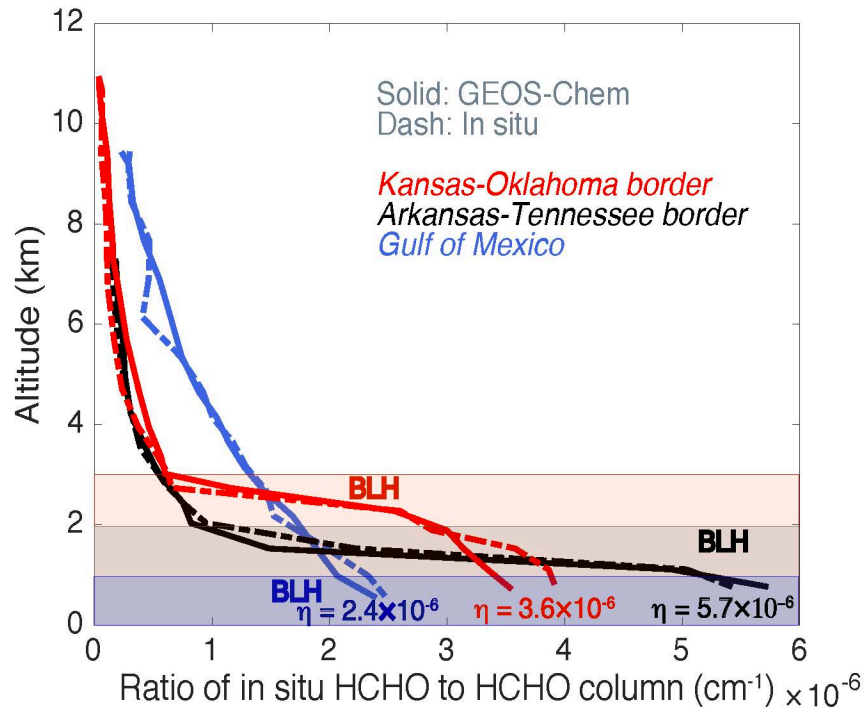
Scatter plots of in situ OA ($\mu\text{g m}^{-3}$) vs. HCHO ($\mu\text{g m}^{-3}$ or molec cm^{-3}) from SEAC⁴RS (excluding biomass burning) (blue), DC3 (dark grey), CalNex (pink), and KORUS-AQ (green) low altitude (< 1 km) data. Inset shows wildfire (brown), and agricultural fire (grey) SEAC⁴RS data. SEAC⁴RS biomass burning cases are defined as acetonitrile > 200 pptv. The linear regression fits are shown as the darker lines and correlation coefficients are provided.



1457
 1458 Figure 3. (a) A scatter plot of OA vs. HCHO for SEAC⁴RS non-biomass burning low
 1459 altitude data color-coded with the product of NO₂ and isoprene in log scale. The red and
 1460 blue lines are the linear regression fits of high (> 0.5) and low (<0.5) product of NO₂
 1461 (ppbv) and isoprene (ppbv), respectively. (b) A scatter plot of OA vs. HCHO for
 1462 KORUS-AQ data color-coded by log(NO₂).
 1463
 1464
 1465

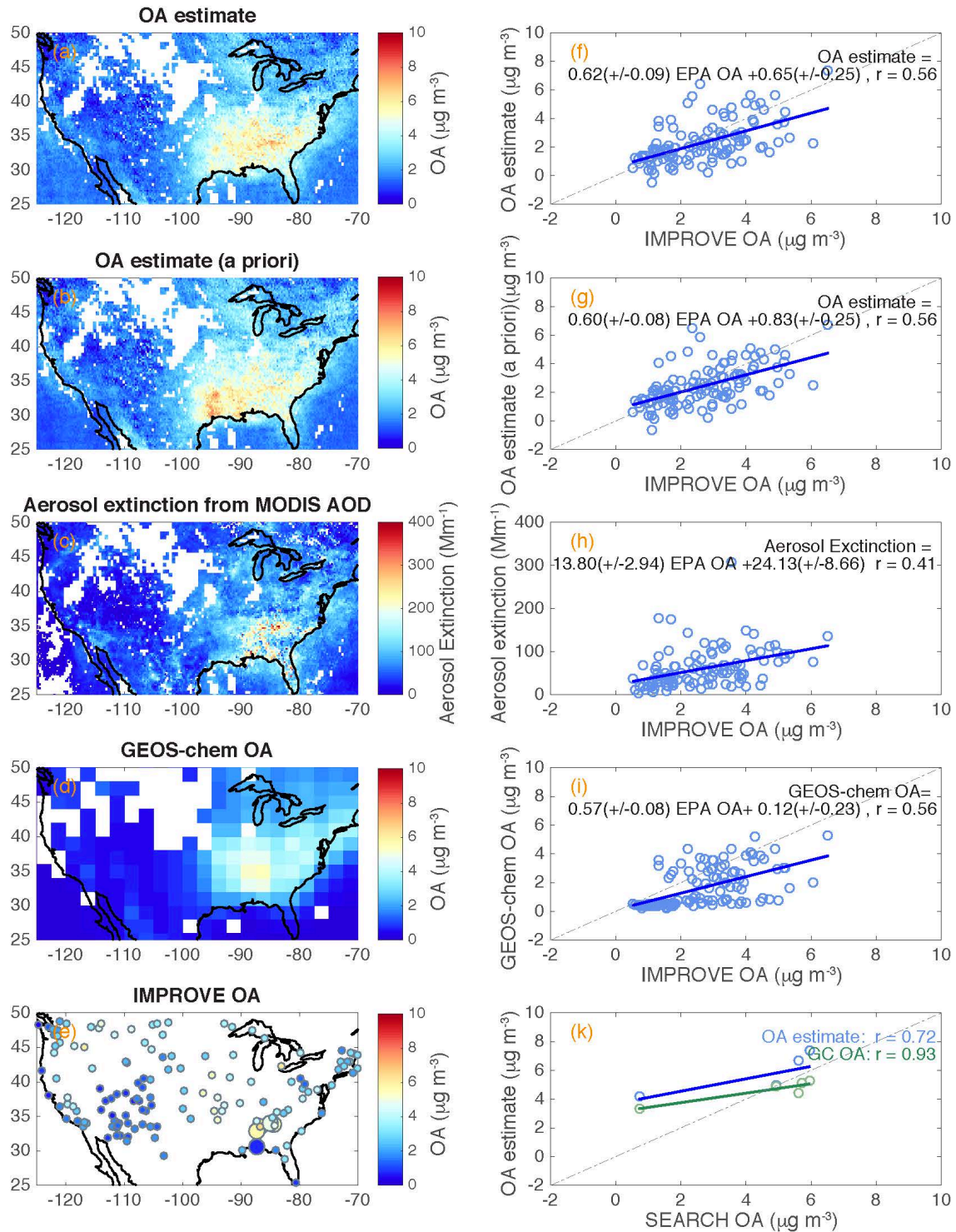


1466
 1467 Figure 4 Scatter plots of OA vs. HCHO for US (SEAC⁴RS altitude < 1 km non-biomass
 1468 burning), South Korea (KORUS-AQ altitude < 1 km) and wildfire (SEAC⁴RS) from in
 1469 situ measurements (a, b, c) and GEOS-Chem outputs sampled along the flight tracks
 1470 (d,e,f).
 1471
 1472



1473
 1474
 1475
 1476
 1477
 1478
 1479
 1480
 1481
 1482
 1483
 1484

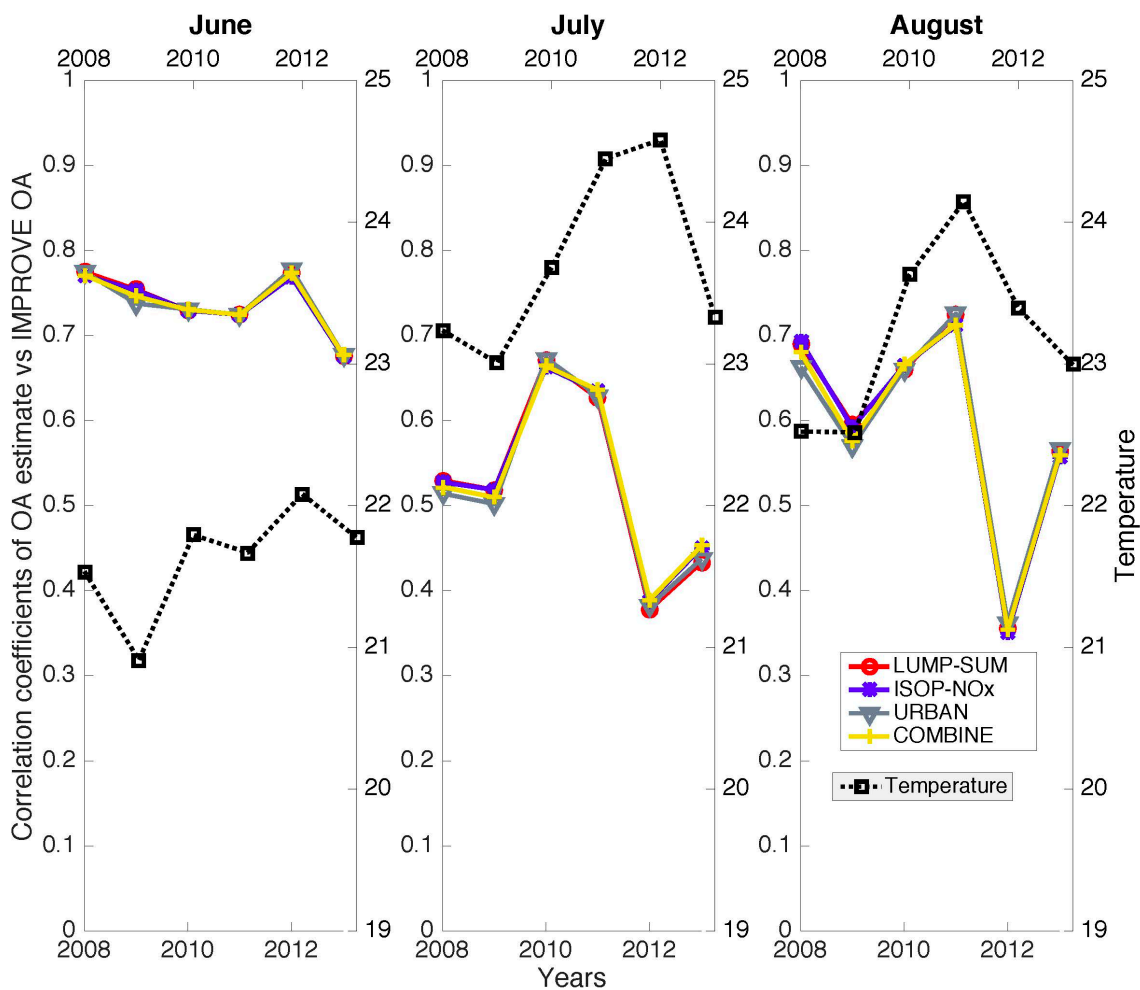
Figure 5. Three typical vertical profiles of the ratio of in situ HCHO concentrations (molec cm^{-3}) to integrated HCHO column from SEAC⁴RS flight track. These three profiles were located at Kansas-Oklahoma border (red), Arkansas-Tennessee border (black), and Gulf of Mexico (blue). Solid curves were from GEOS-Chem results and the dashed were from ISAF measurements. HCHO columns were integrated HCHO concentrations of these vertical profiles extrapolated from 0 to 10 km, assuming the HCHO below and above the measured HCHO vertical profiles were the same as the HCHO at the lowest and highest altitudes sampled, respectively. The boundary layer heights (BLH) of these three profiles are plotted by the shaded areas.



1485
 1486
 1487
 1488
 1489
 1490
 1491

Figure 6. (a) The maps of (a) surface OA estimate (Case 1) with η from GEOS-Chem v9-02, (b) surface OA estimate (Case 1) with η from a priori profiles, (c) surface aerosol extinction derived from MODIS AOD, (d) GEOS-Chem simulated surface OA, and (e) EPA IMPROVE (small dots) and SEARCH (large dots) network ground sites color coded with OA concentrations for August 2013. The scatter plots of (f,g) surface OA estimate, (h) surface aerosol extinction derived from MODIS AOD, and (i) surface GEOS-Chem

1492 OA vs. EPA IMPROVE network ground sites OA. IMPROVE sites OA were corrected
 1493 for evaporation. (k) The scatter plots of surface OA estimate and GEOS-Chem OA vs.
 1494 SEARCH network ground sites OA for August 2013. GEOS-Chem OA and OA estimate
 1495 did not have good correlations with SEARCH OA for other years (SI). For the scatter
 1496 plots, linear regressions are shown (blue and green lines) and regression equations and
 1497 correlation coefficients for the scatter plots are listed. The dashed lines in the scatter plots
 1498 indicate the 1 : 1 line. Biomass burning data (UV aerosol index > 1.6) were excluded in
 1499 all panels.
 1500
 1501
 1502
 1503
 1504



1505
 1506 Figure 7. The correlation coefficients of the linear regression between the OA estimate
 1507 from 4 case (red, blue, gray, and yellow) vs. EPA-corrected OA from 2008 – 2013 for
 1508 June, July, and August. The monthly average ambient temperature is in black.
 1509